

DELFT UNIVERSITY OF TECHNOLOGY

DEPARTEMENT OF TECHNOLOGY

MSc THESIS

---

# Life Cycle Fatigue Damage Estimation for Military Off-Road Vehicles

---

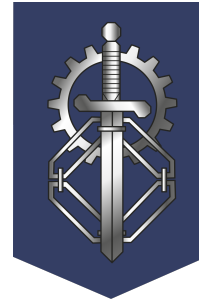
*Author:*

Rick ten Hoopen  
4604768

*Supervisors:*

H.R. van Rijn, MSc  
Dr. Ir. J.C.F. de Winter

March 24, 2022



# Life Cycle Fatigue Damage Estimation for Military Off-Road Vehicles

Author:  
Rick ten Hoopen  
Student 4604768

Supervisors:  
H.R. van Rijn, MSc  
Dr. Ir. J.C.F. de Winter

March 24, 2022

## Abstract

### Introduction

This thesis considers the problem of estimating life-cycle fatigue damage for military off-road vehicles using limited available data. An important durability question is whether military off-road vehicles can cope with the fatigue damage from extreme random, complex, and non-stationary loads for the design life of up to 30 years. We aimed to investigate the accuracy of fatigue damage estimation models by varying the fraction of data used. An accurate life-cycle fatigue damage estimation is essential for military off-road vehicles as the lives of military personnel can depend on a durable vehicle in future use. In addition, minimizing costly data acquisition time leads to a faster validation of a prototype vehicle, which in turn means the vehicle is taken into service faster.

Currently, no comparable publications seem to be available regarding fatigue damage estimation or load extrapolation on (military) off-road vehicles or components. Especially for military applications, reports are often classified or commercially confidential. In addition, some papers contain case studies on operating conditions of utility vehicles, for which road surfaces and loading conditions are not fully comparable to that of (military) off-road vehicles. This study aimed to optimize existing time-domain load extrapolation methods and compare them in fatigue damage to frequency-domain models for military off-road vehicles while minimizing data acquisition time and costs. An error below 5% between the fatigue damage estimations and the validation is deemed satisfactory.

### Method

In total, eight existing fatigue damage estimation models were selected (i.e. two time-domain approaches and six frequency-domain approaches) and the required parameters (e.g. threshold selection, parametric load distribution) were optimized to the varying input data. Fatigue damage calculations in the time-domain is a classical reliable method often considered as benchmark for comparison to frequency-domain models. The two time-domain approaches apply Peak-Over-Threshold load history extrapolation (POT) and Peak-Over-Threshold Rainflow matrix extrapolation (limiting RFM) to complement the lack of extreme loads in the measurements. The selected frequency-domain models performed well on wideband PSDs like automotive spectra in other applications. The six frequency-domain methods implemented were Dirlik (DK), Zhao & Baker (ZB), Ortiz & Chen (OC), Single moments (SM), Tovo & Benasciutti (TB3), and empirical  $\alpha_{0.75}$  method. The eight fatigue damage models were compared in a case study using 270 km of unique off-road strain measurements from a 4x4 light armoured personnel carrier. These measurements represent the actual use in all operating conditions, yet still lack the most extreme events which rarely occur. The dataset was split into a training dataset of 90 km and a validation dataset of 180 km. The parameters of each method were then optimized for a fraction of the training dataset (i.e. 10%, 20%, 40% and 100%) to investigate the

accuracy by calculating the relative error to the benchmark, which is the fatigue damage calculated from the time-domain approach without load extrapolation also called mileage extrapolation (ME). In addition, a generic military off-road PSD-envelope was constructed from the training dataset which was used as a fifth input for the frequency-domain methods to assess accuracy. If the fatigue damage estimation of the PSD-envelope is sufficiently accurate, dynamic modal analysis and fatigue damage can be estimated by only determining the transfer function of the system, thereby eliminating the need for large datasets. Finally, each fatigue damage estimation was validated using the damage calculated from the validation dataset.

## Results

The accuracy of the time-domain approaches is determined from the load spectra comparison and relative fatigue damage error [%] to the mileage extrapolation benchmark. For the frequency-domain approaches only the error in fatigue damage to the ME benchmark was calculated. Finally, for all eight methods the error between the fatigue damage estimations and the fatigue damage from the validation dataset are calculated. The load spectra and fatigue damage error of the POT and limiting RFM to the ME benchmark show that:

- Fatigue damage in the time domain is underestimated up to 32% when only using 10% of the training dataset for ME (i.e. without applying load extrapolation) compared to the full training dataset. The lack of extreme loads in the tail data when using a 10-20% fraction of the training dataset is also clearly visible as discontinuities in the load spectra of the ME and POT method.
- The POT method applied on 10% of the training dataset compensates the fatigue damage underestimation from 32% to an error of 24%, whereas the limiting RFM reduces the error to 18%. A clear and logical trend is visible; the error between POT or limiting RFM and the ME reduces when a larger fraction of the training dataset was used.
- At least 40% of the training dataset was required for a satisfactory accurate fatigue damage estimation of <5% for both time-domain fatigue damage models.
- With the full training dataset as input, the limiting RFM approach gives 0.5% error to the validation fatigue damage, whereas POT showed an error of 4.5%.

Results of the six frequency domain fatigue damage models show that:

- Dirlik's method shows <10% error in validation for 10-20% of the training dataset but overestimates fatigue damage by 14% for larger fractions of the training data.
- TB3 is the most accurate method and is robust when at least 40% of the training dataset is used for input. The minimum error for TB3 was found to be 2.1%, yet this required the PSD from the full training dataset.
- OC overestimate the fatigue damage by 14-27% depending on the fraction of the training dataset used. In addition, the SM method underestimates fatigue damage by 13-17%.
- The generic off-road PSD-envelope gives an error of <3% to the validation data when using the TB3 and empirical  $\alpha_{0.75}$  methods. A comparable error was obtained when applying TB3 and  $\alpha_{0.75}$  to the PSD for the full training dataset.

## Discussion

The aim of this study was to optimize load extrapolation in the time-domain for military off-road vehicles and compare accuracy of all eight fatigue damage models whilst minimizing data acquisition time and costs. Eight existing fatigue damage models were applied on 10%, 20%, 40% and 100% of a training dataset and an off-road PSD-envelope. The accuracy of the models is investigated by the error between the estimation and the normalized fatigue damage from the validation dataset. Both time-domain and frequency-domain models show an error <5% when >40% of the training dataset was used.

The largest factor of influence on the final fatigue damage estimation is the data input. By varying the fraction of the training dataset and calculating the error in fatigue damage to the validation dataset, the influence on accuracy is investigated. Results show significant fatigue damage underestimation for all methods when only 10-20% of the training dataset is used. This is expected since a short time history or corresponding PSD does not contain all information from rare and extreme events. Although validation is performed on a dataset only twice the size of the training dataset, results from all methods show that above a 40% fraction of the training dataset the error compared to the validation stabilizes, indicating the time history contains sufficient extreme loads for an accurate (i.e. <5% error) fatigue damage prediction. For both time-domain load extrapolation methods the input is also determined by the threshold selection method and (non)parametric fit to the exceedances.

Accuracy of the frequency-domain methods depends greatly on whether the assumptions on which the method is developed are valid or not. For example, (semi)empirical approaches are often applicable for a certain range of material parameters and PSD shapes. Other approaches assume the loads to be random, stationary, and Gaussian. All six selected methods performed well on other typical wide-band automotive spectra, yet OC and the SM method did not cope well with this specific off-road truck application compared

to the other methods. TB3 and  $\alpha_{0.75}$  showed the lowest error in validation on  $>40\%$  of the training dataset. Both methods are more recently revised (TB3 in 2006) or developed ( $\alpha_{0.75}$  in 2004) empirical methods fitted to a large variety of PSD samples. Furthermore, the PSD envelope and PSD from the full training dataset show equivalent accuracy for TB3 and  $\alpha_{0.75}$ . This shows potential to use the envelope as input for dynamic modal analysis.

### Conclusions and recommendations

None of the fatigue damage models performed satisfactory for all data fractions of the training set, i.e.,  $<5\%$  error in validation. For at least 36 km of the training dataset, the limiting RFM is the most accurate and computationally efficient time-domain method, whereas BT3 is the most accurate frequency-domain method. The load spectrum from 40% of the training dataset was continuous up to 80% of the maximum value present in the measured time history and provided a validation error  $<5\%$ . It is suggested to use this subjective graphic rule-of-thumb to assess if sufficient extreme loads are present in the measured signal to obtain a fatigue damage estimation error below 5%. The generic PSD-envelope shows comparable accuracy to the PSD from the full training dataset.

In addition to this research, data acquisition time can be reduced further by complementing the extreme and rare events in the measured time history with measurements from an off-road test track where loads are induced at an accelerated rate correlated to the user profile. Also, the graphical methods used for initial threshold selection in the time-domain load extrapolation are subjective, and additions should be made to improve the automated selection procedure. For the frequency-domain approaches, the dependency on material parameters is to be researched since frequency-domain methods are often developed for a specific range. Furthermore, additional research is required to perform dynamic modal analysis and calculate fatigue damage estimates from a generic military off-road PSD. For example, this requires knowledge on the contribution of vehicle parameters, the off-road user profile, and operating conditions to the PSD.

## 1 Introduction

Testing prototype vehicles is costly and time consuming. With fast developments within the automotive branch, manufacturers strive to deliver a reliable and durable product to the market fast. Therefore, testing is often done by simulation parallel to the design phase to save time. Yet, the prototype vehicle still needs to pass tests on the proving ground.

### 1.1 Accelerated Life Cycle Testing

Both reliability and durability are essential aspects to address while testing. Unexpected and premature systematic failures are costly and often lead to recalls, which influence sales numbers due to the affected consumers brand quality opinion [1]. In addition, for military off-road vehicles durability and reliability are more critical since they are required to operate in extreme and often dangerous conditions in remote areas where unexpected failures are difficult to repair. Durability aspects which are often tested include accelerated weathering tests, thermal/climatic testing, buzz, squeek, rattle test and accelerated life cycle testing. In accelerated life cycle testing the main failure mode is fatigue damage caused by cyclic loading of the (sub)structure. Accelerated life cycle testing therefore focuses on fatigue induced wear-out failures at the end of a vehicle's service life as it often leads to catastrophic (component) failure, see figure 1. Several components are economically unattractive to replace if failure occurs and are therefore required to last the service life of up to 20-30 years, e.g. chassis, cabin, axles and other large assemblies. Manufacturers of civilian off-road vehicles stride to simulate the full vehicle durability test, using computer-assisted engineering tools. However, this requires a very accurate and complex multi-body dynamic vehicle and tire model, which is also very time consuming to develop and needs to be validated. Thus, a combination of simulated and actual measured service loads is still often used to make fatigue damage estimations [2]. For off-road military vehicles the nation which procures the vehicle generally performs their own durability tests on the prototype to validate the requirements of the vehicle. Again time is very limited as production is otherwise delayed or the vehicle is taken into service at a later stage thereby influencing operational readiness.

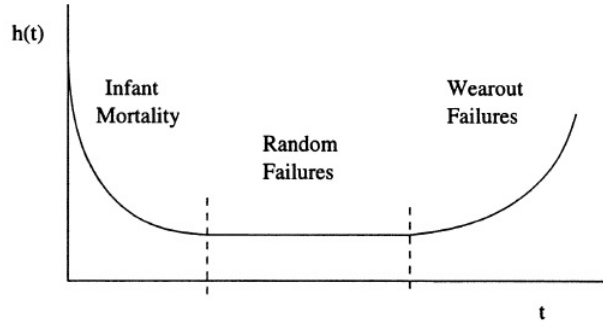


Figure 1: Hazard function, also called 'Bathtub curve' [3]

## 1.2 Fatigue Damage Estimation

Commonly, life-cycle fatigue damage is estimated through load extrapolation of a short measured load history using Rainflow counting combined with a damage accumulation rule or from a known power spectral density (PSD) using frequency-domain methods.

### Time-domain

Time domain fatigue damage estimation spanning the majority of a service life requires a measured load history, often strain, forces, or acceleration measurements. To reduce data acquisition time and costs, a load extrapolation method is required using a short term load history to obtain a service life load history or spectrum. In publications, two main traditional time-domain extrapolation methods are often used and adapted for specific applications: (1) load history extreme value theory (EVT) extrapolation in the time domain [4, 5], and (2) rainflow matrix (RFM) extrapolation using EVT [6, 7, 8]. However, the first challenge is determining a representative short term load history containing all operating conditions. An extrapolation factor of 10-1000 times of the measured load history is not uncommon as limited unique off-road data is available. Furthermore, off-road vehicles, especially for military applications, cope with complex and random non-stationary loads, which makes an accurate long term fatigue damage prediction even more challenging. For military off-road vehicles durability testing standards and procedures are described [9, 10, 11, 12] which focus on classic fatigue damage estimation using an instrumented vehicle to measure a wide variety of loading conditions including the most damaging content from rare and extreme events. After the service loads are obtained and extrapolated, the fatigue damage is calculated using a rainflow counting method, the material S-N or E-N curve, and the Palmgren-Miner linear damage accumulation rule [13]. The rainflow counting algorithm extracts the range and mean of variable load cycles within the time history. The S-N curve is a stress fatigue life model which gives the number of cycles  $N_f$  a standardized specimen can resist up to failure at constant stress amplitude  $s_i$ , see 1, where  $C$  and  $m$  are material properties.

$$N_f s_i^m = C \quad (1)$$

Another fatigue life model is given by the Strain-Life method, which assumes that the strain range  $\Delta\varepsilon$  determines the fatigue response in the structure, see 2.

$$\frac{\Delta\varepsilon}{2} = \frac{\sigma'_f}{E} (2N_f)^b + \varepsilon'_f (2N_f)^c \quad (2)$$

Where  $E$  is the elasticity modulus,  $b$  is basquin's exponent, and  $c$  is the fatigue ductility exponent. In expression 2, both plastic and elastic deformations contribute to fatigue damage contrary to the stress-life model. Thus, for long fatigue life containing primarily elastic deformations, the fatigue strength  $\sigma'_f$  dominates fatigue damage. Whereas, for short fatigue life, plastic deformations dominate fatigue damage through the fatigue ductility  $\varepsilon'_f$  and  $c$ . Finally, the total damage  $D$  induced by the extrapolated or full service load history is calculated using the Palmgren-Miner linear accumulation rule (equation 3), in which  $n_i$  is the number of load cycles within the interval of the signal used, and  $N_f$  is the number of cycles to failure in that interval according to stress- or strain-life model.

$$D = \sum_i \frac{n_i}{N_f} \quad (3)$$

If the accumulated damage  $D > 1$  in the load history failure occurs. Finally, using the accumulated damage  $D$ , and signal time interval  $T_x$  the estimated fatigue life  $T$  is calculated using 4.

$$T = \frac{T_x}{D} \quad (4)$$

### Frequency-domain

Besides extrapolation of the load history or RFM, fatigue damage can be directly estimated from the PSD using spectral moments in the frequency domain [14, 15]. Frequency-based fatigue damage models utilize parameters calculated from the spectral moments about the origin and integrated over the PSD. One key consideration is that also the PSD needs to be representative of all loading conditions as the methods finds a mean damage rate  $\dot{D}$  calculated from the PSD. Many methods are based on compensating a narrow band or wide band solution with an irregularity factor or bandwidth parameter, e.g. [16, 17, 18, 19, 20]. A narrow band signal contains only a few or one frequency, whereas a wide band signal is shot noise and contains many frequencies, see figure 2 for PSD examples. If the signal is falsely assumed narrow band the damage prediction is overestimated, yet for a false wide band assumption the damage is underestimated [21].

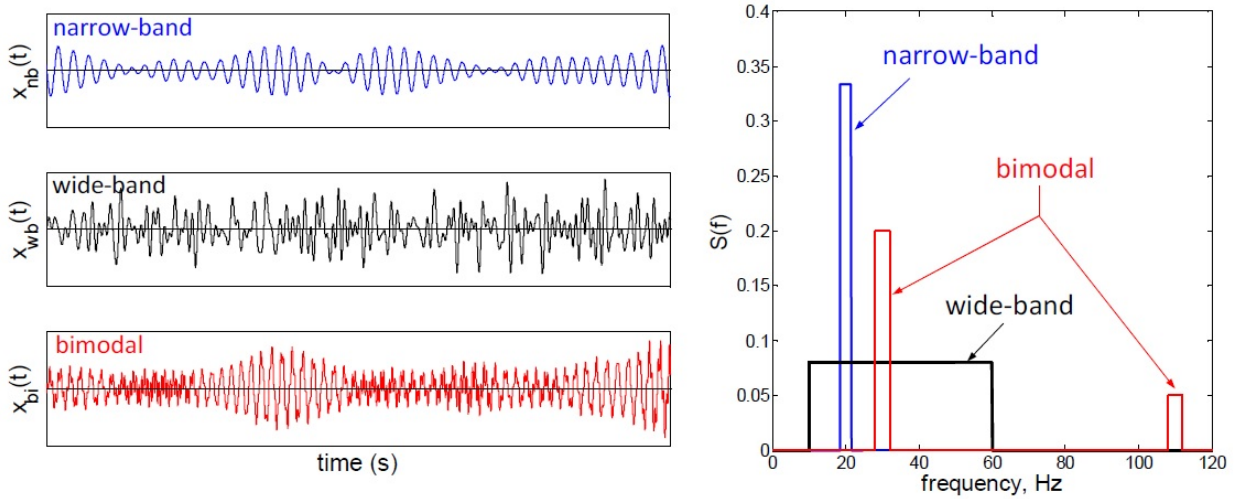


Figure 2: Time history examples for a narrow-band, wide-band, and bimodal signal and the corresponding PSD plots [22]

### 1.3 Problem Statement

There is a paucity on knowledge on how to accurately estimate lifecycle fatigue damage from a short measured load history or PSD. Fatigue damage models are widely reviewed on various PSD shapes or specific applications, yet no comparable publications seem to be available regarding fatigue damage estimation on (military) off-road vehicles or components. In addition, minimizing the measured load history required for an accurate prediction reduces data acquisition time and costs in durability testing. Ideally, an accurate life-cycle fatigue damage estimation is made without performing time-consuming data acquisition using an instrumented vehicle. Therefore, the goal of this thesis was to optimize existing time-domain and frequency-domain fatigue damage estimation methods while minimizing data input for military off-road vehicles. Obviously, accuracy of the estimation is equally important, therefore a maximum error of 5% between the fatigue damage estimation and the validation data is set. The theory behind the applied methods and parameters are presented in chapter 2. Next, the results of a case study using off-road strain measurements from a 4x4 military truck are presented in chapter 3 and validated. Finally, the results from the case study are discussed and concluding remarks and future work are given in chapter 4, and 5, respectively.

## 2 Method

In literature, a wide variety of existing time-domain and frequency-domain fatigue damage estimation methods are implemented, adapted and reviewed for different applications. The load history of a military off-road vehicle shows a tail heavy load distribution and a wide-band PSD. From reviews and applications [22, 23, 24, 25, 26, 27], eight widely used fatigue damage estimation models were selected for the case study in chapter 3. For all eight fatigue damage models described in sections 2.1, and 2.2 below, parameters need to be optimized for the varying input in the case study in chapter 3. The available dataset from the 4x4 military off-road armoured personnel carrier consists of 270 km of strain measurements on the front axle assembly, which is split into a 90 km training dataset and 180 km validation dataset. The input for the case study consists of various fractions, i.e. 10%, 20%, 40% and 100%, from the training dataset. The time-domain approach without load extrapolation, called mileage extrapolation (ME), will serve as benchmark eventhough it is known to be conservative due to the lack of rare and extreme loads. For the time-domain approaches, the normalized load spectra will be compared for analysis of the fatigue damage content per data fraction. Furthermore, the fatigue damage estimations are normalized to the ME from the full training dataset after which the error between the ME and the eight damage estimations is calculated per fraction. In addition, a generic military off-road PSD-envelope is used as a fifth input for the frequency-domain methods to assess accuracy. The overall power in the envelope is equal to that of the PSD from the training dataset. If the fatigue damage estimation of the PSD-envelope is accurate, i.e. <5%, dynamic modal analysis and fatigue damage can be estimated by only determining the transfer function of the system, thereby eliminating the need for large datasets. Finally, the results from the eight fatigue damage models on varying fractions of the training dataset are validated with the remaining subset containing 180 km of strain measurements from the same vehicle in similar conditions.

### 2.1 Time-domain fatigue damage models

Classical time-domain approaches are considered reliable methods for fatigue damage estimation and are used as benchmark to evaluate the performance of frequency domain methods. Since the goal is to minimize data acquisition, the load history or load spectrum needs to be extrapolated to unobserved loads not present in the original signal. The extrapolated signals will be compared in the case study to the results from mileage extrapolation (ME), which is the fatigue damage from the measured time history without load extrapolation scaled to the desired distance or signal length. First, the pre-processing steps performed on the measured time history are explained. Next, the rainflow counting method is presented. The final subsection elaborates on both time-domain load extrapolation methods.

#### 2.1.1 Pre-processing

Before applying extrapolation methods on the measured time history or corresponding load spectrum, the non-damaging and irrelevant content below the fatigue endurance limit is filtered, which also has computational benefits. Let  $X(t) = x_1, x_2, \dots, x_n$ , with  $t \in [0, T]$  be the short term measured load history with sample frequency  $f_s$ , with independent and identically distributed samples of an unknown continuous distribution. First, a band pass filter is applied on  $X(t)$  which filters slow steering corrections  $< 1$  Hz and high frequency vibrations  $> 40$  Hz, which preserves load cycles relevant for automotive fatigue analysis. It is shown by [5, 6] that small amplitude and high frequency cycles only contribute marginally to fatigue damage and therefore can be filtered to reduce computational effort. The *Nyquist sampling theorem* states that  $f_s \geq 2B$  for the frequency  $B$  to be preserved in sampling. However, when applying a rainflow counting algorithm the sample rate needs to be 10-20 times the highest frequency to preserve in order to detect the peaks and valleys in the signal [28]. The sample frequency should therefore be upwards of 400 Hz for off-road vehicle loads. For the case study where  $f_s = 2000$  Hz, this results in a factor 2-5 data reduction.

#### 2.1.2 Rainflow Counting

After filtering, the first time-domain model (POT) directly performs load extrapolation on the measured time history to obtain an extrapolation load history. The second time-domain approach extrapolates the measured RFM, thus after rainflow counting. Using rainflow counting the load distributions of the extrapolated signals can be compared. The method was first introduced by Matsuichi and Endo [29] and counts cycles as closed hysteresis loops by turning the time history into a series of reversals where the signal changes sign. From the reversals, the number and ranges of loading cycles, as well as the mean, are extracted. From the first definition, more than a dozen rainflow counting methods are developed. Newer methods have superseded many older counting methods, which if the time signal starts at the highest peak or lowest trough give the same counts.



Rychlik's definition [30] states that a rainflow range only exists if the signal crosses the level of the current reference peak. Thus checking for previous and future peaks in the signal and only applying the rainflow count when the previous peak value is exceeded. Rychlik's definition is widely used and is shown in figure 3.

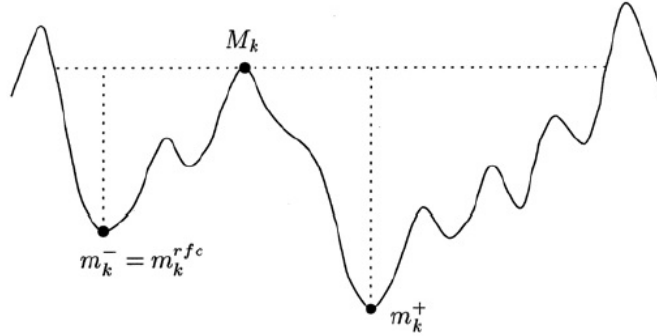


Figure 3: Rychlik's definition of a rainflow range cycle, where the cycle is defined as  $(m_k^{rfc}, M_k)$ , with amplitude  $S_i^{rfc} = (M_k - m_k^{rfc})/2$  [30]

A range-mean plot from the training dataset using Rychlik's rainflow counting method is given in figure 4. Finding the load distribution of the resulting range and mean from rainflow cycle counting is a multivariate

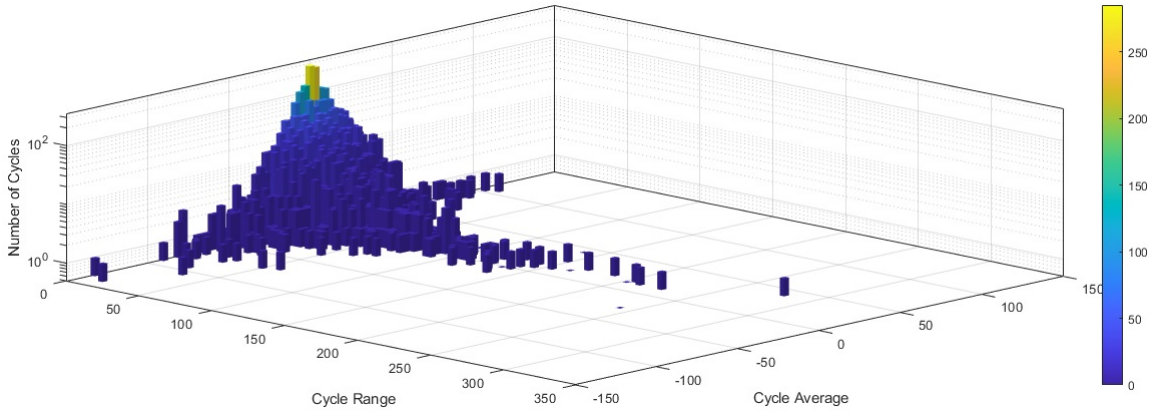


Figure 4: Range-mean histogram containing 4483 cycles derived from the training dataset by Rychlik's definition of rainflow cycle counting.

problem. Since the mean stress affects fatigue strength significantly [31] stress correction is applied to obtain zero-midpoint equivalent stress ranges, thereby reducing the problem to a univariate case. The relation proposed by Marin [32] is generalized in expression 5.

$$\left(\frac{\sigma_a}{\sigma_{ar}}\right)^n + \left(f\frac{\sigma_m}{\sigma_u}\right)^m = 1 \quad (5)$$

With  $\sigma_a$ ,  $\sigma_{ar}$ ,  $\sigma_m$ ,  $\sigma_u$  the original stress amplitude, corrected stress amplitude, original mean stress and ultimate tensile strength, respectively. Multiple mean correction methods are developed on this general expression of which the values are given in table 1 [33]. Where  $\sigma_y$ , and  $\sigma_{fB}$  are the yield strength and true fracture strength, respectively. The true fracture strength can be replaced in Morrow's method for  $\sigma'_f$ , which is the physical limit to  $\sigma_m$ .



Method	Values
Goodman	$n = 1, m = 1, f = 1$
Gerber	$n = 1, m = 2, f = 1$
Dietman	$n = 2, m = 1, f = 1$
Soderberg	$n = 1, m = 1, f = \frac{\sigma_u}{\sigma_y}$
Morrow	$n = 1, m = 1, f = \frac{\sigma_u}{\sigma_{fB}}$

Table 1: Mean stress corrections in stress-life fatigue

### 2.1.3 POT Load Extrapolation

Since the ME is performed on an incomplete load distribution from a fraction of the training dataset, EVT is applied to correct the estimation. The tail of the load distribution contains large uncertainties due to the lack of data, especially for short time histories. EVT extrapolates only extreme loads to complement the lack of tail data. Four methods are available of which three are applied on a time history and one extrapolates the measured RFM. The first time-domain approach is peak-over-threshold (POT), which defines a threshold level and fits an excess distribution function to the exceedances above the threshold. The second is block-maxima-method (BMM) which divides the time history into equal blocks and models the probability of the maximum (or minimum) in each block. The method-of-independant-storm (MIS) is the third time-domain method and combines POT and BMM by also defining a threshold within the signal blocks, which in this methods are events (storms). Since BMM and MIS require large sample sizes as they only utilize a small fraction of the available data, they are not suitable for off-road data and not considered any further. The limiting RFM approach is similar to the POT-method, except it is applied to the extreme values of the measured RFM in stead of the time history.

### Generalized Pareto Distribution

For the POT-method a threshold needs to be selected to separate the bulk and tail of the load distribution. Next, a suitable tail model needs to be fitted. As shown by [34], and [35] the tail model or conditional excess distribution function follows a Generalized Pareto Distribution (GPD) for sufficiently high thresholds, as graphically illustrated by [36] in figure 5. Considering the exceedances  $y_i$  of  $X(t)$  above a threshold level  $u$ , i.e.:

$$y_i = x_i - u, \text{ for } x_i > u \quad (6)$$

The conditional excess distribution function  $F_u(y)$  of the exceedances is then given by expression 7.

$$F_u(y) = P(X - u \leq y | X > u) = \frac{P(X - u \leq \wedge X > u)}{P(X > u)} = \frac{F(u + y) - F(u)}{1 - F(u)} \quad (7)$$

The cumulative distribution function (CDF) and probability density function (PDF) of the GPD are defined in 8 and 9, where the parameters  $\xi$  and  $\sigma$  of are called the shape and scale parameter, respectively.

$$F(x|\mu, \xi, \sigma) = \begin{cases} 1 - (1 + \xi \frac{x-\mu}{\sigma})^{-\frac{1}{\xi}} & , \xi \neq 0 \\ 1 - \exp(-\frac{x-\mu}{\sigma}) & , \xi = 0 \end{cases} \quad (8)$$

$$f(x|\mu, \xi, \sigma) = \begin{cases} \frac{1}{\sigma} [1 + \xi (\frac{x-\mu}{\sigma})]^{-1+\frac{1}{\xi}} & , \xi \neq 0 \\ \frac{1}{\sigma} \exp(-\frac{x-\mu}{\sigma}) & , \xi = 0 \end{cases} \quad (9)$$

In the limiting case, the GPD reduces to an exponential distribution for  $\xi = 0$  and  $\mu = 0$  or a Pareto distribution when  $\xi > 0$  and  $\mu = \sigma/\xi$ .

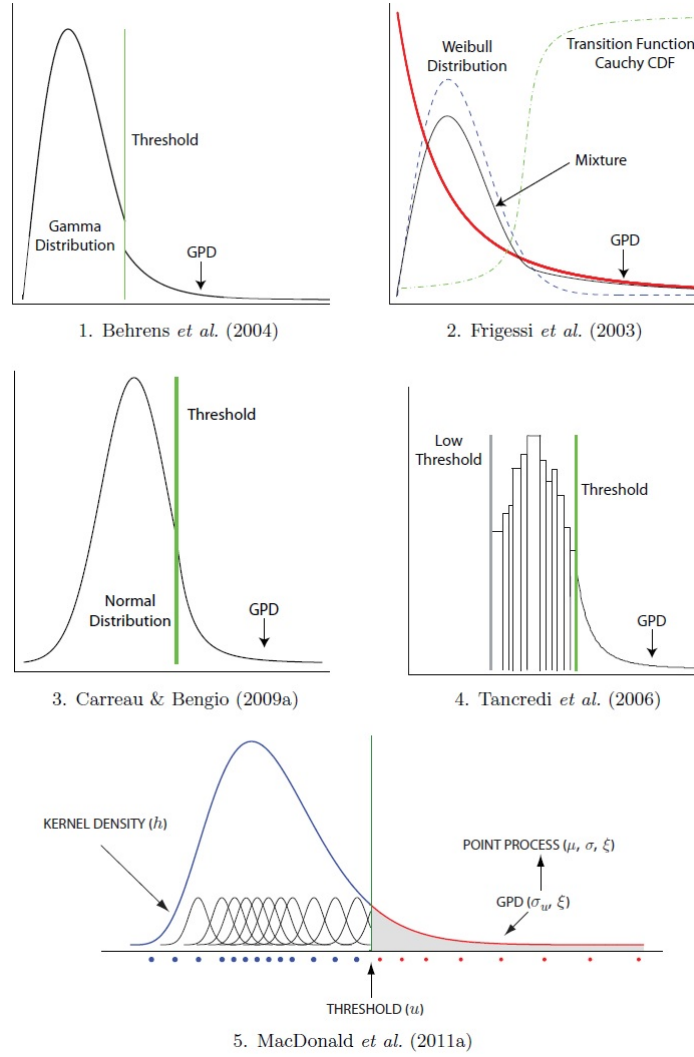


Figure 5: Examples of extreme value mixture models with a GPD-tail distribution.

### Threshold Selection

Before generating more data regarding the extreme and random loads in the tail of the PDF, a proper threshold needs to be selected for which the GPD tail model assumptions hold. Many threshold selection methods are developed using graphical methods, computational methods, rules of thumb, or a combination of those methods. Determining the threshold is a trade-off between variance and bias. The variance increases as a result of the reduced sample size. However, a sufficiently high threshold is required to make the assumed GPD tail model valid, thereby reducing bias [36]. Traditional graphical methods to estimate the threshold require experience and are subjective, e.g. the Mean Residual Life plot (MRL) and threshold stability plot [37]. The MRL-plot shows the mean of the exceedances versus threshold, which is approximately linear for a GPD [38]. Suppose the measurements  $x_1, x_2, \dots, x_k$  are a subset of the time history  $X$  of which  $k$  observations exceed the possible threshold  $u_0$ . The mean excess function is given by

$$e(u) = E(X - u | X > u) = \frac{\sigma_{u0} + \xi u}{1 - \xi} \quad (10)$$

For a threshold  $u_0$  the excesses follow a GPD, then for all  $u > u_0$  the resulting GPD has the same shape, yet shifted scale  $\sigma_u = \sigma_{u0} + \xi(u - u_0)$ . The expectation of the exceedances for  $(X - u) \sim \text{GPD}(\sigma, \xi)$  is given by 11. Hence, by verifying the empirical mean excess function is linear in  $u$  the threshold can be graphically selected.

$$e_n(u) = \frac{1}{k} \sum_{i=1}^k (x_i - u) \quad (11)$$

In the threshold stability plot, the MLE of the shape parameter  $\xi$  is calculated and plotted against the number of exceedances and the threshold. For the specific case where  $\xi > 0$  and the GPD is a Pareto Distribution, the Hill estimator [39] is often used as maximum likelihood estimator for the power coefficient  $\alpha = -\xi$ . The likelihood function for the power coefficient  $\alpha$  is given by:

$$L(\alpha, x_i) = \prod_{i=1}^{\infty} \alpha \frac{x_m^\alpha}{x_i^{\alpha+1}} = \alpha^n x_m^{n\alpha} \prod_{i=1}^{\infty} \frac{1}{x_i^{\alpha+1}} \quad (12)$$

Where  $x_m$  is the mean of  $x$ . Taking the partial derivative of the logarithmic likelihood function with respect to  $\alpha$  and set this equal to zero we get the Hill estimator  $H_k$ .

$$H_k = \alpha^{-1} = \frac{1}{k} \sum_{i=1}^k \log x_{(n-i+1)} - \log x_{(n-k)} \quad (13)$$

In all graphic methods, the lowest threshold value is chosen which still results in a good tail model fit. For large datasets graphical methods can be time-consuming. Therefore, constant quantile levels preserving fatigue damage content or pre-determined (physical) thresholds are chosen if applicable. However, in applications there are often many suitable threshold, which are not taken into consideration when choosing a fixed threshold. In addition to fixed thresholds, several rules of thumb have been developed, e.g. fitting Pareto tails to the 10th and 90th percentiles by [40], or selecting  $k = \sqrt{N_0}$  as suggested by [41, 42] or  $k = N_0^{2/3} / \log[\log(N_0)]$  by [43], where  $N_0$  is the number of cycles in the signal.

### Limiting Rainflow Matrix

The ME benchmark for the case study is the measured RFM  $\mathbf{F}$  scaled by a desired factor to represent a service life load history, however this doesn't capture all loading conditions. To solve this issue, the limiting RFM  $\mathbf{G}$  is constructed from an estimation for extreme values (i.e. the tail), and the measured RFM  $\mathbf{F}$  normalized by distance elsewhere. Often, a smoothing technique, e.g. (a)KDE smoothing, is also applied to the bulk of the measured RFM. The limiting RFM is given by:

$$\mathbf{G} = (g_{ij})_{i,j=1}^n, \text{ with } g_{ij} = \lim_{z \rightarrow \infty} \frac{E[f_{ij}]}{z} \quad (14)$$

Where  $f_{ij}$  are the number of cycles in the measured RFM regarding  $z$  km. Calculation of the limiting RFM  $\mathbf{G}$  by directly estimating a model for the loads is often not possible due to the lack of available data in the tail. However, the area of interest for fatigue damage is the tail of the model. Finding  $\mathbf{G}$  which only fits the tail accurately is therefore essential for fatigue damage estimation. Calculating the limiting RFM  $\mathbf{G}$  for extreme loads is therefore done by extracting the number of level upcrossings from the measured RFM  $\mathbf{F}$ . The level upcrossing spectrum  $N$  is extrapolated to unobserved levels using POT. The upcrossings of a high or low level (threshold) are assumed to converge into two independent Poisson processes [44, 45]. Furthermore, Rychlik's definition of the Rainflow count [30] states that a cycle with a minimum below  $u$  and maximum above  $v$  only exist if the values are exceeded in both directions in the signal, which is equivalent to upcrossing the interval  $[u, v]$  of the time history  $X(t), t \in [0, T]$ . The intensity  $\mu$  of the number of upcrossings  $N_T(u, v)$  is given by

$$\mu(u, v) = \lim_{T \rightarrow \infty} \frac{N_T(u, v)}{T} \quad (15)$$

For an ergodic process, the upcrossing intensity  $\mu(u, v)$  of the closed interval  $[u, v]$  is equal to that of the cumulative rainflow intensity  $\mu^{rfc}(u, v)$ . Johannesson [7] showed that for a threshold with a GPD-tail distribution a good approximation for the upcrossings intensity is given by

$$\mu^{rfc}(u, v) \approx \frac{\mu(u)\mu(v)}{\mu(u) + \mu(v)} \quad (16)$$

To apply the POT-method on the the measured RFM  $\mathbf{F}$  the level upcrossing spectrum  $N$  can be calculated using

$$N = (n_k)_{k=1}^n, \text{ with } n_k = \sum_{i < k < j} f_{ij} \quad (17)$$

Where only cycles exceeding the threshold are summed. The level upcrossing spectrum can be used to identify a threshold based on quantile levels. Secondly, using  $N$  the exceedances are derived and the parameters  $\xi$ , and

$\sigma$  of the GPD are estimated using the MLE. Finally, the limiting RFM  $\mathbf{G}$  is estimated using equation 18 and the approximation for the cumulative rainflow intensity 16.

$$\mathbf{G} = (g_{ij}^{rfc})_{i,j=1}^n, \text{ with } g_{ij}^{rfc} = \mu_{i+1,j-1}^{rfc} - \mu_{i,j-1}^{rfc} - \mu_{i+1,j}^{rfc} + \mu_{i,j}^{rfc} \quad (18)$$

Johannesson [7] showed that the limiting RFM  $\mathbf{G}$  gives good results for extreme values. Yet, the threshold choice remains essential for the fitted GPD. Furthermore, for the bulk of the distribution or the cycles below the threshold the estimation is not valid. Thus a suitable bulk model is still required.

### (Adaptive) Kernel Density Estimation

As rainflow matrices rarely follow a parametric distribution, one option is to apply a kernel smoothing function on  $\mathbf{F}$  below the threshold to obtain the empirical normalized RFM of all loading conditions. Kernel smoothing is achieved by convolution of an estimator with a kernel  $K$ . Considering the samples  $X$ , representing zero midpoint rainflow ranges, from the unknown probability distribution  $f$ . The kernel density estimate (KDE) for a 1-dimensional problem is shown in expression 19 [46].

$$\hat{f}_h(x) = \frac{1}{nh} \sum_{i=1}^n K\left(\frac{x - X_i}{h}\right), \quad (19)$$

where  $h$  is the bandwidth and  $K$  is the kernel function of which several examples are given below. For  $\hat{f}_h(x)$  to be a pdf, the kernel  $K$  needs to satisfy:

$$\begin{aligned} K(x) \leq 0, \quad K(x) = K(-x) \\ \int_{-\infty}^{\infty} K(x)dx = 1, \quad \int_{-\infty}^{\infty} xK(x)dx = 0, \quad \int_{-\infty}^{\infty} x^2K(x)dx < \infty \end{aligned} \quad (20)$$

In addition the scaled kernel  $K_h$  is given by 21, which reduces 19 to 22

$$K_h(u) = h^{-1}K(h^{-1}u) \quad (21)$$

$$\hat{f}_h(x) = \frac{1}{n} \sum_{i=1}^n K_h(x - X_i). \quad (22)$$

For KDE, the choice of kernel  $K$  has less influence on the estimation than the bandwidth parameter  $h$ . However, a uniform kernel can give very jagged edges in the estimation resulting in undesirable discontinuities [46]. Several examples of univariate kernels are given in table 2.

Kernel	$K(x)$
Normal	$(2\pi)^{-\frac{1}{2}} \exp \frac{1}{2}x^2$
Epanechnikov	$\left(\frac{3}{4}\right)(1 - x^2)\mathbb{1}_{( x <1)}$
Uniform (box)	$\frac{1}{2}\mathbb{1}_{( x <1)}$
Biweight	$\left(\frac{5}{16}\right)(1 - x^2)^2\mathbb{1}_{( x <1)}$
Triweight	$\left(\frac{35}{32}\right)(1 - x^2)^3\mathbb{1}_{( x <1)}$
Triangular	$(1 -  x )\mathbb{1}_{( x <1)}$

Table 2: Popular univariate kernels

The problem of selecting the bandwidth  $h$  is crucial for an accurate estimation as it affects smoothing of data. If the bandwidth is too small, undersmoothing occurs resulting in small bias and large variance. Furthermore, oversmoothing from a large bandwidth results in large bias and small variance. To prevent under- or oversmoothing, the optimal bandwidth is calculated by minimizing the global error criterion; the Mean Integrated Squared Error (MISE) given in 23, also called the  $L_2$  loss function.

$$MISE = E \left[ \int_{-\infty}^{\infty} (\hat{f}_h(x; h) - f(x))^2 dx \right] \quad (23)$$

Finding the optimal bandwidth  $h$  is generally not possible with 23, since  $f(x)$  is unknown. A large sample approximation of the MISE is required by Taylor series expansion. Under the assumptions that  $f'' \neq 0$  and  $\mu_2 \neq 0$ , 23 can be rewritten into:

$$\text{MISE} = \text{AMISE} + o((nh)^{-1} + h^4),$$

$$\text{AMISE} = (nh)^{-1}R(K) + \frac{1}{4}h^4\mu_2(K)^2R(f''), \text{ with} \quad (24)$$

$$R(K) = \int K(x)^2 dx, \mu_2(K) = \int x^2 K(x) dx, R(f'') = \int f''(x)^2 dx$$

AMISE is the asymptotic MISE and is the large sample approximation. The minimum AMISE and corresponding bandwidth  $h_{\text{AMISE}}$  is found by differentiating with respect to the bandwidth  $h$  and set this equal to zero:

$$\frac{\partial}{\partial h} \text{AMISE} = -\frac{R(K)}{nh^2} + \mu_2(K)^2 h^3 R(f'') \quad (25)$$

$$h_{\text{AMISE}} = \left( \frac{R(K)}{\mu_2(K)^2 R(f'') n} \right)^{\frac{1}{5}}$$

The trade-off between bias and variance is clearly shown in 24, where the first term of the AMISE is the variance and converges at a rate proportional to  $(nh)^{-1}$ . To minimize the variance the bandwidth  $h$  should be large. However, convergence of the bias is proportional to  $h^4$ , which suggest  $h$  should be as small as possible. Since the true density function  $f$  is unknown, equation 23, and 25 cannot be used directly. Therefore, many bandwidth selection methods are suggested, e.g. rule-of-thumb, cross-validation, or plug-in selectors.

Yet, a fixed KDE can perform poorly in sparse data regions like the tail of an off-road vehicle load spectrum. Using adaptive kernel density estimation can provide a more accurate model. Shimazaki & Shinomoto [47] suggested to iteratively find the optimal bandwidth within local intervals using a stiffness constant  $\gamma$ . The stiffness constant is defined as a ratio of the optimal fixed bandwidth to a length of a local interval in which a fixed-kernel bandwidth optimization was performed. The steps are as follows:

1. Identify data representing all loading conditions
2. Calculating the local cost function in 27 for possible bandwidth  $h$  for interval  $w$ .
3. Repeat previous step and vary the interval  $w$ , using the stiffness parameter  $\gamma$ , around observation  $x_i$  for all observations. ,
4. Find optimal interval length  $W_\gamma$  and bandwidth  $h_\gamma$  within that interval by calculating and minimizing the cost function.

For the algorithm described above the cost function to be minimized for a Gaussian kernel and the MISE from expression 23 is given by:

$$C(h, w) = \hat{f}_h(x; h)^2 - 2\hat{f}_h(x; h)f(x) + \frac{2/w}{\sqrt{2\pi}}f(x) \quad (26)$$

The possible interval lengths are scaled according to

$$W = \gamma^{-1}\hat{w} \quad (27)$$

As explained in [47], small  $\gamma$  results in a bandwidth optimization of a long interval, whereas for  $\gamma \sim 1$  the interval in which the bandwidth is optimized is short. The approach using the stiffness parameter gives locally optimized bandwidths within scaled and shifted intervals. Hence, the resulting intervals overlap and require smoothing. The Nadaraya-Watson kernel regression is applied to achieve a smooth density estimate from a locally weighted average using weights which sum up to 1.

## 2.2 Frequency-domain fatigue damage models

Computational effort becomes a serious aspect in load extrapolation in the time-domain [48]. Furthermore, it is expensive to collect a sufficiently long load history containing all loading conditions. Thus selecting an accurate frequency-based fatigue damage model is preferred but requires the PSD of the load history. Models based on the PSD assume that the variable amplitude random loading is a sequence of stationary processes, which for real applications isn't exactly true. Frequency based fatigue damage models for stationary, random and Gaussian processes provide direct and computationally efficient damage estimations from spectral moments calculated from the PSD. The PSD from a time signal is calculated using 28, where  $L_s$  is the length of the time history.

$$G_k(f) = 2L_s [(realX_k)^2 + (imagX_k)^2] \quad (28)$$

Main benefit from spectral methods are the computational efficiency compared to time domain fatigue damage estimation methods. However, for comparison and verification in chapter 3 on off-road vehicle loads a synthesized timeseries from the PSD is also constructed which in this case counteracts the improved computational efficiency. Many frequency-domain fatigue damage models have been developed, which are often suitable for a specific range of material parameters or PSD shapes. Examples of frequency-domain fatigue damage estimation methods are given below. From the available methods six methods are selected on good performance on wideband (automotive) PSD plots, which are indicated bold.

- Wirsching and Light (1980) [16],
- **Dirlik (1985) [20]**
- **Ortiz and Chen (1987) [17]**,
- **Larsen and Lutes 'Single Moments' (1990) [18]**
- **Zhao and Baker (1992) [49]**
- Fu-Cebon (2000) [50]
- **Tovo and Benasciutti (2002, 2005, 2006) [51], [19], [52]**
- **Benasciutti, empirical  $\alpha_{0.75}$  method (2004) [53]**
- Gao and Moan (2008) [54]
- Lalanne (2009) [55]

Fatigue damage in the frequency-domain calculated with the S-N curve and Miner cumulative damage rule is defined as:

$$D = \nu_p T C^{-1} \int_0^\infty s^k p(s) ds \quad (29)$$

With  $s$  the rainflow amplitudes,  $p(s)$  the cycle amplitude PDF,  $C$  the Basquin material constant from equation 1, and  $T$  is the desired time duration. Since  $p(s)$  is essential in the damage estimation yet unknown it needs to be estimated using spectral moments calculated from a single sided PSD using 30.

$$M_j(f) = \int_0^\infty f^j G_k(f) df \quad (30)$$

Where  $f^j$  is the frequency of order  $j$  and  $G_k$  is the single sided PSD from 28. The PSD is often discontinuous and needs to be numerically integrated to obtain the spectral moments. Statistically, the zero order moment  $M_0$  is the variance and  $\sqrt{M_0}$  is the standard deviation. From the selected models, the methods Ortiz & Chen (OC), Single Moments (SM), Tovo-Benasciutti from 2006 (TB3), and empirical  $\alpha_{0.75}$  all compensate a narrowband solution of 39. However, the methods from Dirlik (DK) and Zhao & Baker (ZB) estimate  $p(s)$  with a mixture model.

### 2.2.1 Narrowband correction methods (OC, SM, TB3, $\alpha_{0.75}$ )

For a narrowband extreme load distribution, Bendat [56] assumed the rainflow amplitude of each cycle is symmetrical and the PDF follows a Rayleigh distribution. Which defines the narrowband fatigue damage as:

$$D_{NB} = \nu_0 C^{-1} T(\sqrt{2M_0})^m \Gamma\left(\frac{1}{2}m + 1\right) \quad (31)$$

Where  $\Gamma$  is the gamma function and  $m$  is the fatigue slope exponent. As mentioned in chapter 1, a narrow band signal contains only one or a few frequencies, whereas a wideband signal is like shot noise and contains many frequencies. If the signal is falsely assumed narrowband the damage prediction is overestimated, yet for a false wideband assumption the damage is underestimated. Automotive spectra cannot be assumed narrowband and thus require correction. Many proposed methods apply a correction factor  $\zeta$  to the narrowband damage estimation  $D_{NB}$  using bandwidth parameters  $\alpha_i$ :

$$\alpha_i = \frac{M_i}{\sqrt{M_0 M_{2i}}} \quad (32)$$

In which for  $i = 2$  the irregularity factor  $\gamma$  is given, calculated with the expected rate of upcrossing  $\nu_0$  and the average rate of peaks  $\nu_p$ . For  $\zeta \sim 1$  the result is narrowband, and for  $\zeta \sim 0$  the damage corresponds to a wide-band process. The irregularity factor  $\gamma$  is given by

$$\gamma = \frac{\nu_0}{\nu_p} = \frac{\sqrt{\frac{M_2}{M_0}}}{\sqrt{\frac{M_4}{M_2}}} = \frac{M_2}{\sqrt{M_0 M_4}} \quad (33)$$

The first correction method by Ortiz & Chen suggests to compensate 31 with  $\zeta_{OC}$ , which is developed using the generalized spectral bandwidth  $\beta_k$ . The term  $M_k$  is the numerical integration of 30 of order  $2/m$ .

$$\zeta_{OC} = \frac{\beta_k^m}{\alpha_2}, \text{ with}$$

$$\beta_k = \sqrt{\frac{M_2 M_k}{M_0 M_{k+2}}} \quad (34)$$

$$k = 2/m$$

The second frequency-domain method using a narrowband correction is the single moment (SM) method suggested by Lutes and Larsen, which compensates  $D_{NB}$  by

$$\zeta_{SM} = \frac{\left(\frac{M_k}{M_0}\right)^{m/2}}{\nu_0}, \text{ with} \quad (35)$$

$$k = 2/m$$

Additionally, the third method given by Tovo-Benasciutti (TB3) seeks a linear combination between  $D_{NB}$ , which is often an overestimation, and the rainflow count fatigue damage approximated from the compensated narrowband damage using  $\gamma$  from 33. The approach requires four spectral moments and was fitted to 286 sampled PSD's. Tovo-Benasciutti suggested:

$$\zeta_{TB} = b + (1 - b)\alpha_2^{m-1} \quad (36)$$

The initial parameter  $b$  has been improved twice in later studies, and are given below. The parameters  $\alpha_1$  and  $\alpha_2$  are calculating using 32. The third definition (TB3), based on  $b_3$  is used later on in the case study.

$$b_1 = \min\left(\frac{\alpha_1 - \alpha_2}{1 - \alpha_1}, 1\right)$$

$$b_2 = \frac{(\alpha_1 - \alpha_2)[1.112(1 + \alpha_1\alpha_2 - (\alpha_1 + \alpha_2))e^{2.11\alpha_2} + (\alpha_1 - \alpha_2)]}{(1 - \alpha_2)^2} \quad (37)$$

$$b_3 = \frac{\alpha_{0.75}^2 - \alpha_2^2}{1 - \alpha_2^2}$$



The final narrowband correction method is also from Benasciutti. The empirical  $\alpha_{0.75}$  method is given by:

$$\zeta_\alpha = \alpha_{0.75}^2 \quad (38)$$

### 2.2.2 Dirlik (DK)

The Dirlik method is developed from 70 PSDs of various shapes which were normalized to the same rms value and expected rate of peaks  $\nu_p$ . From the PSDs time histories were generated using IFFT. After applying a rainflow counting algorithm the PSDs were related to the PDF of the rainflow ranges. The suggested PDF consists of a mixture of an exponential and two Rayleigh distributions [20], which is given by:

$$p(Z) = \frac{1}{2\sqrt{M_0}} \left[ \frac{D_1}{Q} e^{-\frac{Z}{Q}} + \frac{D_2 Z}{R_2} e^{-\frac{Z^2}{2R_2^2}} + D_3 Z e^{-\frac{Z^2}{2}} \right] \quad (39)$$

Where  $r$  are the rainflow ranges,  $Z$  is the normalized rainflow ranges defined as  $Z = \frac{r}{2\sqrt{M_0}}$ , and the parameters  $D_1$ ,  $D_2$ ,  $D_3$ ,  $Q$ , and  $R$  are defined as:

$$D_1 = \frac{2(X_m - \gamma^2)}{1 + \gamma^2}$$

$$D_2 = \frac{1 - \gamma - D_1 + D_1^2}{1 - R}$$

$$D_3 = 1 - D_1 - D_2 \quad (40)$$

$$Q = \frac{1.25(\gamma - D_3 - D_2 R)}{D_1}, \text{ with}$$

$$X_m = \frac{M_1}{M_0} \sqrt{\frac{M_2}{M_4}}, \quad R = \frac{\gamma - X_m - D_1^2}{1 - \gamma - D_1 + D_1^2}$$

### 2.2.3 Zhao and Baker (ZB)

Zhao and Baker (ZB) combined theoretical assumptions and simulation to define the PDF of the rainflow ranges, which consists of a linear combination of a Weibull and Rayleigh PDF:

$$p(Z) = w\alpha\beta Z^{\beta-1} e^{-\alpha Z^\beta} + (1-w)Z e^{-\frac{Z^2}{2}} \quad (41)$$

The parameters  $w$ ,  $\alpha$ , and  $\beta$  are expressed as:

$$w = \frac{1 - \alpha_2}{1 - \sqrt{\frac{2}{\pi}} \Gamma\left(1 + \frac{1}{\beta}\right) \alpha^{-\frac{1}{\beta}}}$$

$$\alpha = 8 - 7\alpha_2 \quad (42)$$

$$\beta = \begin{cases} 1.1 & , \alpha_2 < 0.9 \\ 1.1 + 9(\alpha_2 - 0.9) & , \alpha_2 \geq 0.9 \end{cases}$$

The first element in the PDF estimate of the ZB-method (41) is the Rayleigh distribution for large rainflow ranges, the second element is the Weibull distribution for small ranges. The ZB method is not applicable for  $\alpha_2 < 0.13$ , otherwise  $w > 1$  which gives incorrect results. Furthermore, preferably  $2 \leq m \leq 6$  as the model is simulated for those values. The improved ZB-method, also called ZB2, is not considered as the method is for developed for  $m \approx 3$  whereas  $5 < m < 8$  is a default range for steels in military applications as described in [12].

### 3 Case Study

The data for the case study consist of 270 km of unique strain measurements from the front axle assembly of a 4x4 armoured personnel carrier. The full vehicle details and user profile are military confidential, therefore limited vehicle specifications are given in table 3. The dataset contains 17 samples with different operating

Combat weight	15000	kg
Vehicle Width	2.5	m
Vehicle length	7.2	m
Vehicle height	2.7	m
Wheelbase	3.9	m
Track width	2.1	m

Table 3: Specifications of the 4x4 military off-road vehicle

conditions (surface type, vehicle speed, etc) specified in the off-road user profile which is military confidential. This dataset is split into a training dataset of 90 km and a validation set of 180 km by splitting each of the 17 samples in the corresponding ratio. For the case study eight fatigue damage models are selected and optimized for a 10%, 20%, 40% or 100% fraction of the training dataset to examine when the fatigue damage content of rare and extreme events within the sample is insufficient and leads to an inaccurate (i.e. above 5% error) fatigue damage estimation. The eight fatigue damage models are:

1. POT extrapolation (POT)
2. Limiting RFM (lim RFM)
3. Ortiz & Chen (OC)
4. Single Moments (SM)
5.  $\alpha_{0.75}$  (a75)
6. Tovo & Benociutti 3 (TB3)
7. Dirlik (DK)
8. Zhao & Baker (ZB)

First, the experimental setup used for data acquisition of the strain measurements is illustrated. Secondly, the effects of the pre-processing steps are shown. Next, the two time domain fatigue damage models are implemented and the load extrapolation is optimized for a 20% fraction of the training dataset. The procedure for the other sample fractions is equal, yet other parameters are found to be optimal. Following, the PSD-plots of the samples and the PSD-envelope are presented for the six frequency-domain fatigue damage models. Finally, the results of the load spectra comparison of the time-domain models are presented along with the errors in fatigue damage estimation of all eight models and are validated with the validation dataset in the final section.

#### 3.1 Experimental setup

Data acquisition was performed with an instrumented vehicle using strain gauges with a linear pattern and a 90°shear/torque rosette pattern combined with a portable data collection system. The bridge circuits of the linear strain gauges were completed using bridge completion modules at the measuring location of the strain gauge, see figure 6. The linear strain gauge was applied on the front axle, rear axle, shock absorber mounts and main chassis beams on both the left and right side of the vehicle. The shear/torque rosette strain gauges were applied on the front and rear chassis crossmembers for which the bridge circuit is completed within the data collection system. Datasheets [57, 58] are added in appendix A. Measurements from a linear strain gauge on the left side of the front axle are used in the case study.

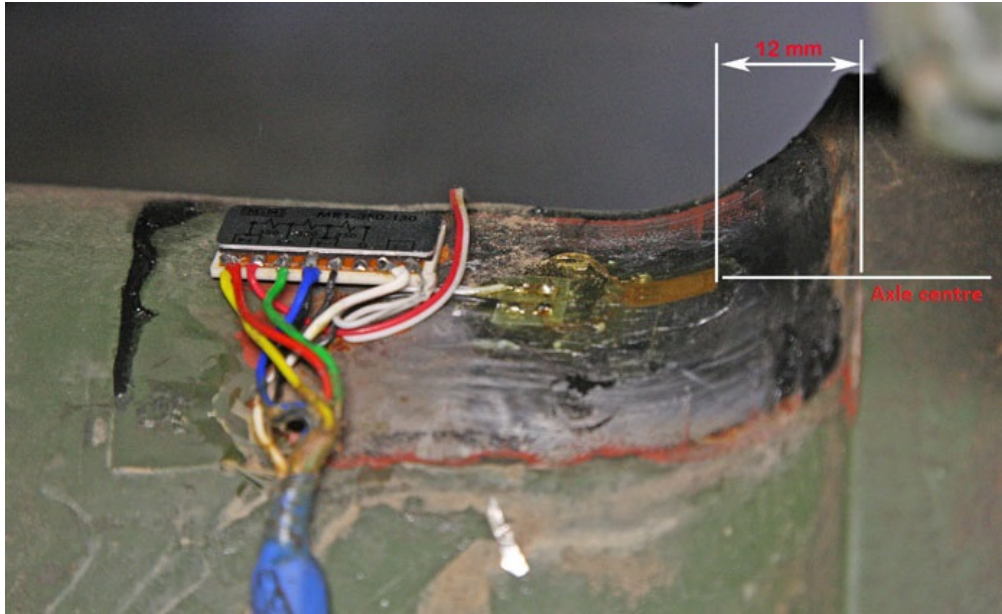


Figure 6: Linear strain gauge and bridge completion module on the left side of the front axle of the military 4x4 armored personnel carrier.

### 3.2 Pre-processing

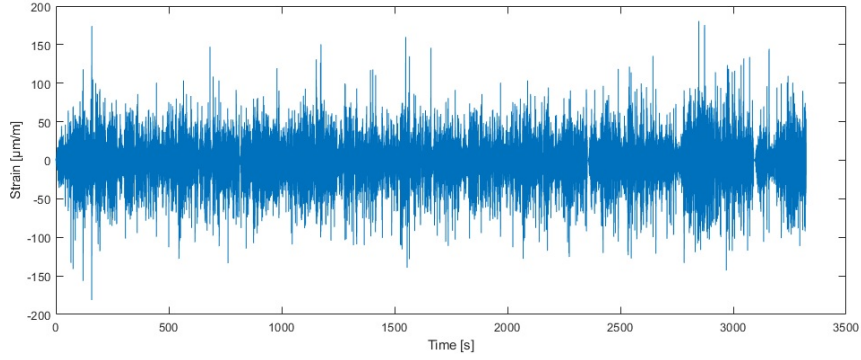
The strain load history used in this case study are imposed on the vehicle through the tire-surface contact patch by driving over disturbances from road section varying from block pavement to cobble stone roads and even rock terrain, see appendix B for surface examples [59, 60]. A required speed was pre-determined and adapted by the driver if needed for comfort or safety. The 20% fraction of the training load history after pre-processing including filtering is given in figure 7, where 7b shows the desired content for the rainflow counting is preserved after resampling. The damaging content of the sample is analyzed before optionally removing non-damaging content for computational purposes. Figure 8 shows the RFM of the sample and which load cycles contribute the most in fatigue damage. The damage from figure 8b accumulated and scaled to desired length is equivalent to the ME approach without load extrapolation. Clearly, even though the tail of the distribution lacks data, the few extreme and rare loads contribute significantly more to the fatigue damage accumulation than the many but small load cycles. If computational problems arise when extrapolating in the time domain one can choose to remove the smallest load cycles as they contribute marginally to the fatigue damage. By applying the band-pass filter and re-sampling from section 2.1 the original data size is already reduced by a factor five. Yet, when extrapolating up to a 1000 times, further data reduction by removing small load cycles may be required. For the most accurate results one should preserve as much content as possible also taking into consideration that the sequence of loading affects the fatigue damage induced on the structure [61]. Additionally, the Goodman correction is applied to compensate for alternating loads with a non-zero midpoint to obtain zero-midpoint equivalent loads [62], thereby reducing the load spectrum to two dimensions and simplifying load extrapolation.

### 3.3 Time-domain fatigue damage models

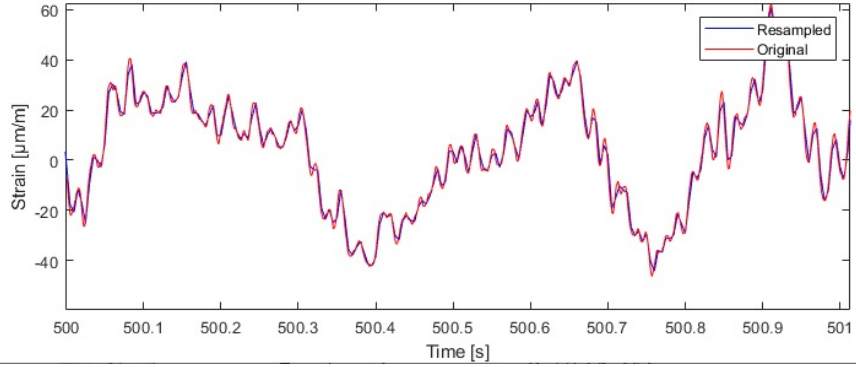
In this section the POT load extrapolation method is applied on both the measured time history and the measured RFM. The 20% fraction from the training dataset is used as sample. For all data fractions the optimization steps below were executed.

#### 3.3.1 Time history extrapolation

The first step for the POT-method is threshold selection, after which the extreme values surpassing the threshold are resampled from the fitted GPD distribution. In order to select a suitable initial threshold for the POT-method, the Mean Residual Life plot and Threshold Stability Plot are graphically inspected. Secondly, possible thresholds linearly spaced around the initial threshold are defined. For each possible threshold, three parametric tail models (i.e. GPD, exponential, and Weibull distribution) are fitted to the exceedances for comparison. The final fit and threshold are selected on the minimum mean squared error (MSE).



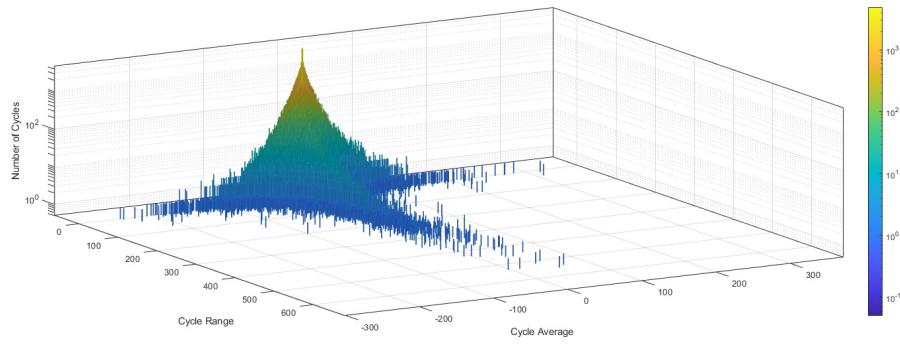
(a) Load history from a 20% or 18 km training sample.



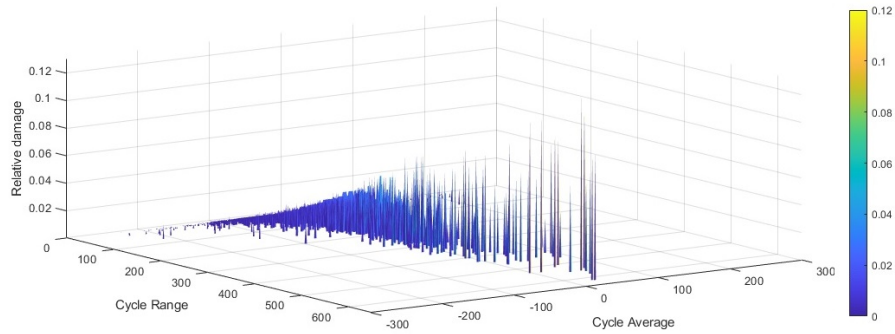
(b) Zoomed section of figure 7a showing the effect of resampling with  $f_s = 400Hz$ .

Figure 7: Training data strain load history measured on the front axle assembly of a 4x4 military truck in unloaded condition while driving on various off-road surfaces.

To assist in selecting a value for the threshold  $u$ , the mean residual life (MRL) plot or mean excess plot was produced for values starting at zero, see figure 9. For the GPD to be a good fit for the tail model, the MRL-plot should be linear in the threshold as mentioned in section 2.1.3. As the MRL-plot shows a linear relation for all possible thresholds one can assume the parametric GPD fit for the entire load distribution. However fitting on the entire load distribution often shows greater errors in the tail, which is the region of interest containing rare and extreme loads. Accuracy of the tail fit for a large and low threshold is shown in appendix C and D.



(a) Rainflow count.



(b) Relative damage contribution.

Figure 8: Distribution and fatigue damage content of load cycles in original strain time history.

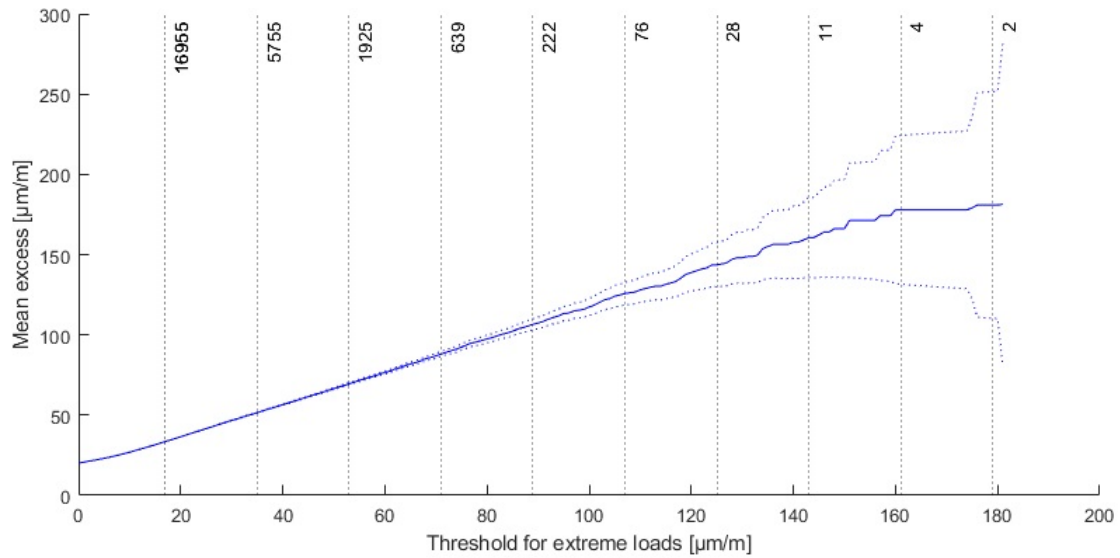


Figure 9: Mean Residual Life plot from a 20% training sample containing off-road strain measurements measured on the front axle of a 4x4 military truck. The dotted blue lines show 95% confidence intervals and the dotted black lines show the number of exceedances with the corresponding threshold.

The MRL-plot shows that at three possible thresholds (i.e. 80, 95 and 116  $\mu m/m$ ) the slope changes indicating a transition to the rare and extreme values. The other changes in slope where  $u > 130\mu m/m$  cannot be considered reasonable as they result in an insufficient number of exceedances to accurately fit the extreme load distribution. For each sample, a good initial thresholds from the MRL-plot can be identified and the error of the fit on the extreme load distribution is calculated, which is minimized later on when the exact threshold is determined. The lowest possible threshold is selected to preserve a high number of extreme values, thereby

reducing variance. When reducing the amount of input data by a factor 3-5, the shape of the MRL-plot and thereby initial threshold selection method remain fairly unchanged which indicates the extreme loads are evenly distributed among the various off-road sections driven. Yet, with a shorter time sample fewer exceedances remain for a good fit on the tail distribution. The corresponding threshold stability plot (TSP) in figure 10 shows for both positive and negative exceedances the MLE of the scale parameter. The MLE of the shape parameter  $\xi$  remains constant and stable up to  $75 \mu m/m$  for positive, and  $92 \mu m/m$  for negative exceedances, respectively. The suitable initial thresholds from the TSP are in agreement with the MRL-plot.

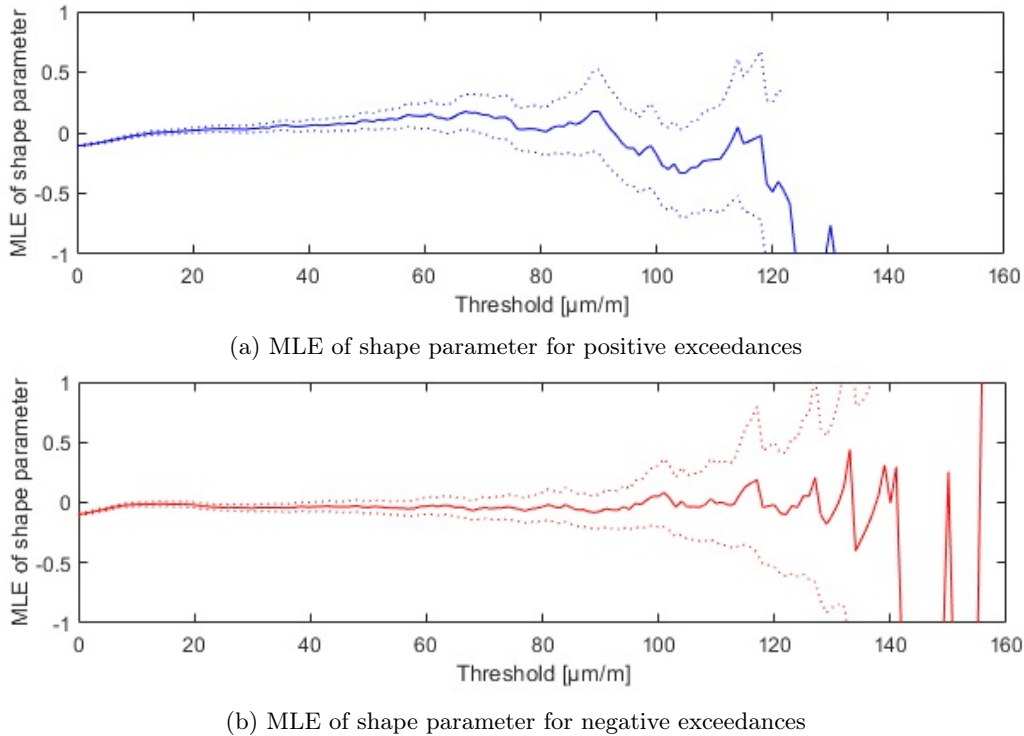


Figure 10: Threshold stability plots of the shape parameter from a GPD-fit versus possible thresholds applied to 20% of the training dataset containing strain measurements of a military off-road vehicle. The dotted lines show 95% confidence intervals.

To find the optimal threshold, the MSE between the empirical exceedance distribution and fitted (Weibull, exponential or GPD) distribution is calculated for linearly spaced possible threshold around the initial threshold options found from the MRL- and TSP-plots. The distribution and threshold with the lowest error is selected, which for 20% of the training dataset was a GPD with thresholds  $78$  and  $-95 \mu m/m$  for positive and negative exceedances, respectively. The optimal thresholds differs for each sample of the training dataset used and are given in table 4.

Sample of training dataset	10%	20%	40%	100%
$u_{max} [\mu m/m]$	73	78	90	98
$u_{min} [\mu m/m]$	-84	-95	-104	-110

Table 4: Optimal thresholds for different sample sizes of the training dataset.

For the 20% sample, the mean squared errors (MSE) of the fit on the exceedances are given in table 5. Selection on the MSE suggests the GPD for both negative and positive exceedances.



Distribution	MSE <sup>+</sup> ( $\times 10^{-4}$ ) $u = 0$	MSE <sup>+</sup> ( $\times 10^{-4}$ ) $u > 78$	MSE <sup>-</sup> ( $\times 10^{-4}$ ) $u = 0$	MSE <sup>-</sup> ( $\times 10^{-4}$ ) $u > 78$
Exponential	24.00	4.26	9.32	2.50
Weibull	1.00	4.41	1.17	2.38
Generalized Pareto	14.00	4.00	5.47	2.32

Table 5: MSE for fitted distributions on the positive and negative exceedances above threshold  $u$  of the 20% training dataset.

Since the MRL-plot is approximately linear for all  $u$ , this suggests a low (or no) threshold is also possible. Thus, we consider all three parametric distributions, i.e. Weibull, Exponential, and Generalized Pareto, to fit on the entire sample (i.e.  $u = 0 \mu m/m$ ) and just the tail data (i.e.  $|x| \geq u$ ). The fit is shown together with the empirical CDF and squared errors in appendix C and D. The parametric distributions fitted to the full load history show greater errors in the tail of the distribution compared to the parametric distribution only fitted to the exceedances, thereby providing more accurate results when extrapolating. The optimal shape- and scale parameter of the GPD-fit on the positive exceedances are set to  $\kappa = -\xi = 0.0417$ , and  $\sigma = 16.448$ . For the GPD fit on the negative exceedances the shape and scale parameters are  $\kappa = -\xi = -0.0240$ , and  $\sigma = 18.809$ , respectively. The low values for the shape parameter indicate that the fit is close to exponential where  $\kappa = 0$ . Figure 11 shows satisfactory comparison between the empirical and fitted distribution. In addition, it shows the lack of available tail data and an unexpected high probability for positive exceedances around  $100 \mu m/m$ , which are confirmed by a graphical goodness of fit assessment from the probability- and quantile plot in appendix E. Detailed analysis shows that the data deviates significantly between positive and negative exceedances. For instance, there are less positive exceedances than negative, namely 166 versus 302. Yet, the positive exceedances have higher absolute maxima, which confirms a separate fit for positive and negative exceedances is required.

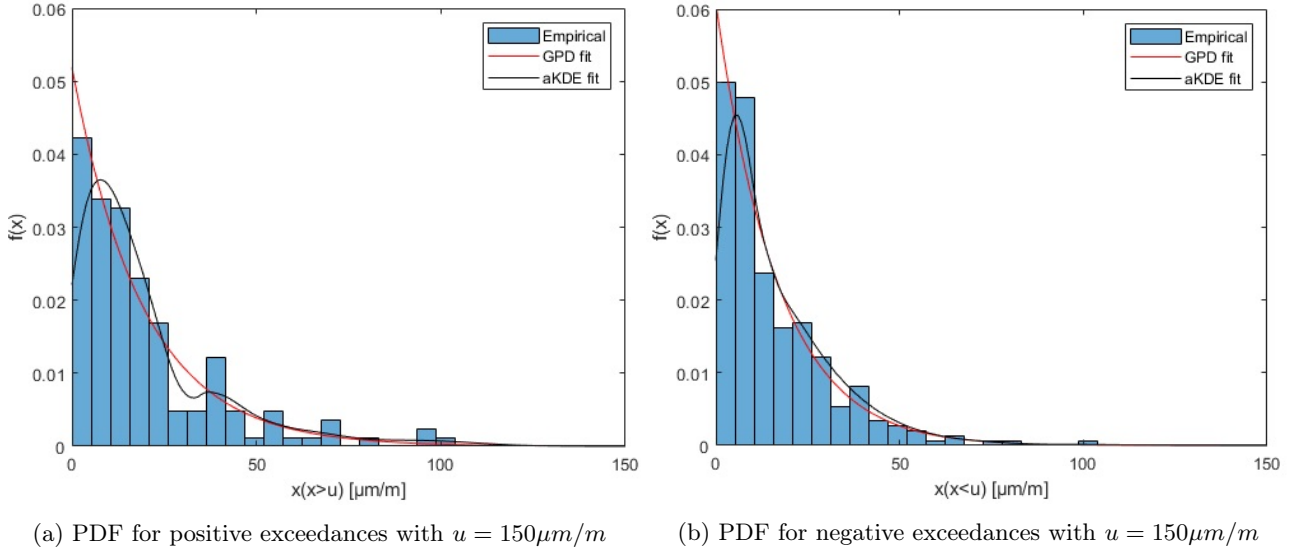


Figure 11: Empirical PDF, non-parametric aKDE, and parametric GPD fit on extreme loads of a 20% training sample from strain measurements. The measurements were performed on the front axle assembly of a military 4x4 off-road truck.

Figure 11 also displays the result from a non-parametric fit on the exceedances using aKDE, see section 2.1.3. Since an aKDE does not assume any shape of the PDF it is able to suit the dataset better, yet it is also more sensitive to outliers. The aKDE shows slightly higher probability overall for negative exceedances. However, for the positive extreme values the same aKDE method overfits on the data with a narrow bandwidth. The dip in the lower ranges is due to the aKDE being applied on just the exceedances for comparable probabilities. Considering one of the objectives of this thesis is to select a robust extrapolation method on a very limited amount of data, the parametric fit is considered favorable as it is less sensitive to outliers and more suitable for a tail with low data density.

After threshold selection and fitting a parametric distribution to the extreme values, the final step is copying the load history and randomly resample only the positive and negative exceedances from the fitted GPDs. As suggested by [42], the original time history is extrapolated a factor 10 or higher to obtain a load history



representing all loading conditions. A fraction of the time history containing resampled exceedances is shown in figure 12.

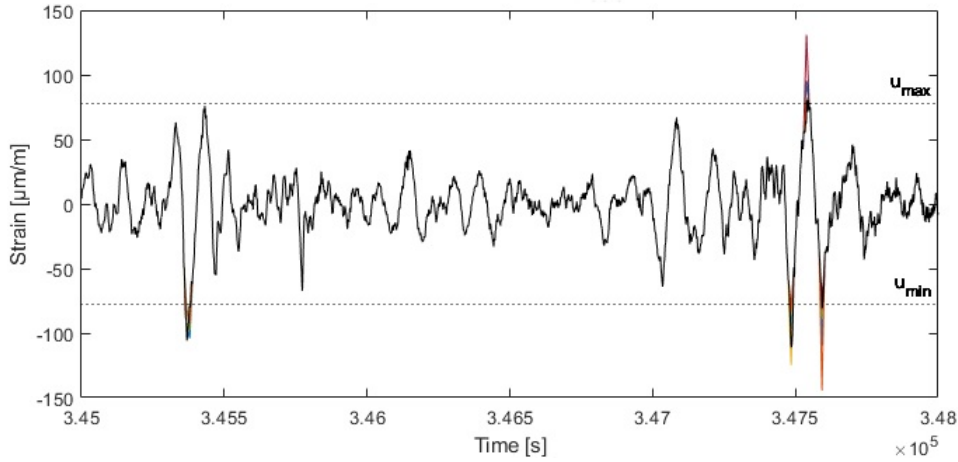


Figure 12: Time interval of a 20% strain measurement training sample capturing the original signal (black) and five times POT extrapolation (other colors) above the threshold  $u_{max}$  and below  $u_{min}$ .

Every simulation will provide slightly different results, since the POT extrapolation method is based on a random simulation of the extreme values from the fitted exceedance distribution. Next, rainflow cycle counting is applied and the mean strain is corrected in the strain range or amplitude. The result is a two dimensional load spectrum shown in figure 13, where the zero values are removed for readability.

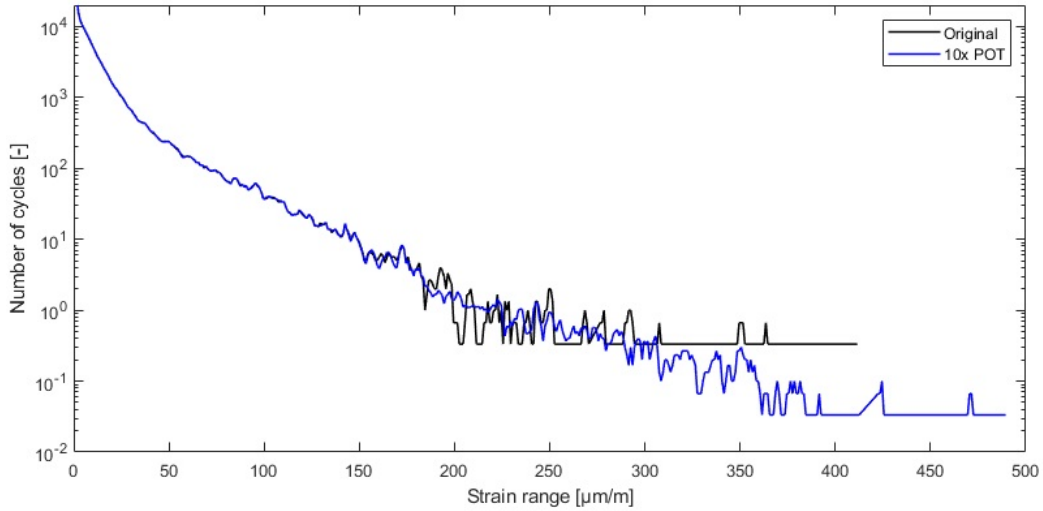


Figure 13: Load spectrum of the sample (i.e. 20% training data) and 10 times POT extrapolated load history.

### 3.3.2 RFM extrapolation

As an alternative to applying the POT-method on the time history, the limiting RFM can be constructed for extreme values from the measured RFM. Working in the rainflow domain is more efficient than the time domain as it doesn't result in long time histories for large extrapolation factors. The limiting rainflow matrix describes the shape of the rainflow matrix for extreme values containing fatigue damage content from all loading conditions, i.e. loads above the threshold. The method is based on the asymptotic theory of (extreme) load level crossings, as described in section 2.1.3 and also applies the POT-method. First, the original level upcrossing spectrum is calculated from the measured rainflow matrix in which the cycles below the fatigue endurance limit are neglected and thus rainflow filtered. Next, the level upcrossings are extrapolated to higher unobserved load levels using the POT-method, see figure 14. As figure 14 shows, a lower extreme of  $-421.5 \mu\text{m}/\text{m}$  and a high extreme load of  $403 \mu\text{m}/\text{m}$  occur once for an extrapolation factor of 100, i.e.  $10^{-2}$  upcrossings.

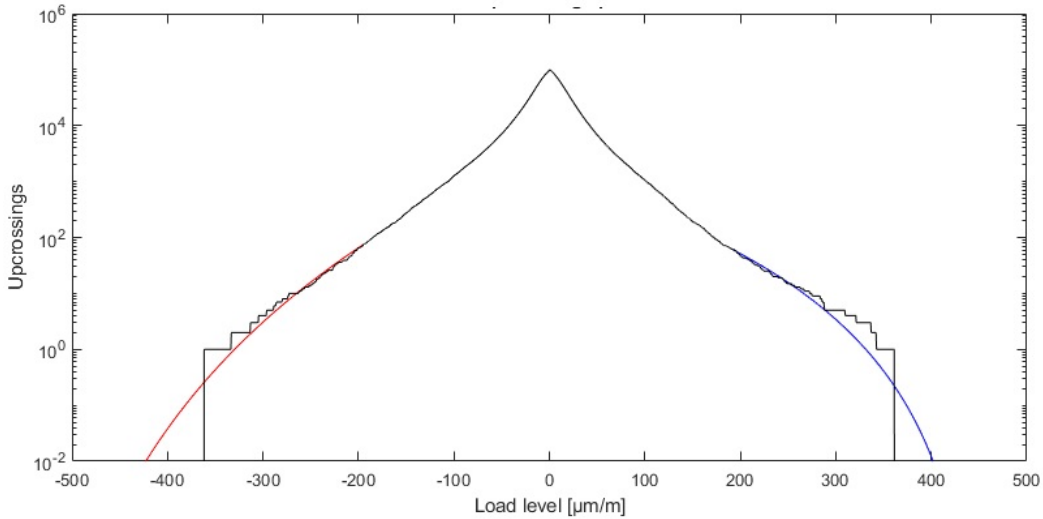


Figure 14: Upcrossing spectrum from a 20% training data sample and GPD extrapolation of the extreme positive (blue) and negative (red) load levels.

In contrary to the time domain approach where minimizing the M(I)SE combined with graphical methods was used for threshold selection, the threshold is now set using a rule of thumb and verified using the same graphical methods. The threshold is set for 5% of the sample that crosses the maximum value of the upcrossing spectrum as suggested by [7]. Thresholds and parameters of the fitted GPDs are given in table 6. Using the extrapolated

Parameters	threshold [ $\mu m/m$ ]	$\kappa$	$\sigma$
Positive load levels	191.7	-0.184	48.45
Negative load levels	-193.8	-0.0978	38.40

Table 6: Fitted GPD parameters on the level upcrossing spectrum of the 20% sample from the training dataset.

upcrossing spectrum, the extreme RFM is calculated using equations 16 and 18. Finally, the limiting RFM  $\mathbf{G}$  consists of two separate RFM's; 1: the RFM for extreme extrapolated load levels which is only valid above the threshold, and 2: the original or (a)KDE smoothed RFM elsewhere. The limiting RFM  $\mathbf{G}$  using 20% of the training dataset is shown in figure 15. Clearly, the extrapolated extreme RFM envelops the rare extreme cycles in the tail of the distribution nicely and allows for other cycles to be present for high extrapolation factors. Furthermore, in figure 15 the asymmetric curved shape of the limiting RFM estimate in the extreme values is coherent with the fact that there are more negative extremes present in the measured load history. Unfortunately, smoothing the bulk of the RFM also smoothens the values below the line  $y = x$ , which is an unwanted effect. The arrays in the final limiting RFM  $\mathbf{G}$  should therefore be set to zero.

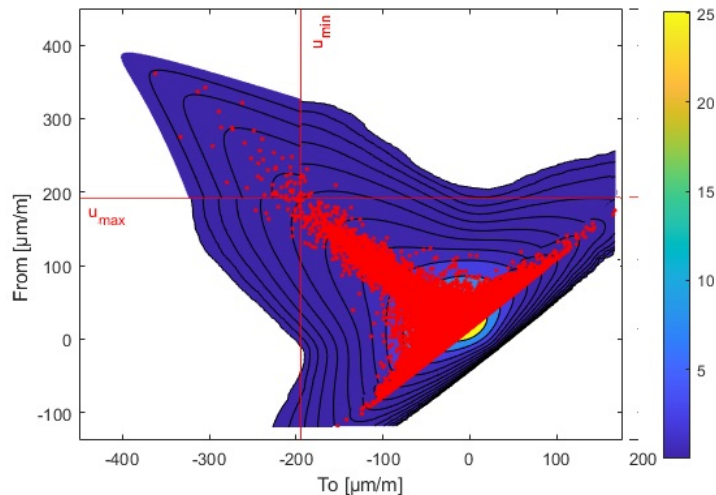


Figure 15: Limiting RFM  $G$  from a 20% training sample measured on the front axle of a military off-road truck. The extrapolated extreme RFM is valid above  $u_{max}$  and below  $u_{min}$ , and the aKDE smoothed RFM is used elsewhere. The limiting RFM is shown in isolines, whereas the original rainflow cycles are shown as red dots.

### 3.4 Frequency-domain fatigue damage models

Frequency-domain load extrapolation methods use spectral moments calculated from the PSD, as explained in detail in section 2.2. The input PSD is calculated from the corresponding time sample so all methods have the same input. It is also desirable to compare the PSD approach to the time-domain methods in load spectra. Therefore, a synthesized load history can be generated from a PSD. As described by [24], the PSD input is multiplied with perfect white noise before IFFT to synthesize a time series with an equivalent PSD shape and amplitude. However, the load spectrum of the PSD generated time history does not provide reasonable results, see fig 17. The PSD's and time histories of the original and synthesized signal are compared and validated in appendix F, which show the loading sequence is falsely neglected and needs to be taken into account. Since this information is unknown when only the PSD is used as input it is impossible to reconstruct the load sequence of the extreme ranges. This method is therefore not considered any further.

The PSD from the training dataset sample, a 10 times POT extrapolation, and a generic military off-road PSD-envelope are given in figure 18. The off-road truck PSDs show good agreement in shape with typical wideband automotive spectra as shown in [25]. The PSD from the POT extrapolation shows the frequencies where damaging content is added by complementing the tail of the load distribution. Furthermore, the PSD-envelope is suggested to be used as a fifth input (besides the PSDs from the four training dataset fractions) for the frequency-domain methods to assess accuracy. If the fatigue damage estimation of the PSD-envelope is sufficiently accurate, dynamic modal analysis and fatigue damage can be estimated by only determining the transfer function of a new system and correlating the user profile to an PSD-envelope, thereby eliminating the need for large datasets.

### 3.5 Results

The results of the case study are shown in figure 16 and table 7. First, graphical analysis of the load spectra for time-domain fatigue damage models allows to quantify the underestimation of ME and how well the load extrapolation methods compensate the lack of rare and extreme loads. Next, the eight fatigue damage estimations from the 10%, 20% and 40% samples are normalized to the result from the full training dataset and the error between ME and the other methods is calculated to investigate trends and identify which estimations are within the 5% error tolerance.

#### 3.5.1 Load Spectra

Figure 16 clearly shows where the PSD extrapolated time history deviates from the original time history caused by neglecting the load sequence resulting in an inaccurate fatigue damage estimation as explained in appendix

F. The load spectrum of the original sample shows that the data density in the tail becomes sparse from around  $190 \mu\text{m}/\text{m}$  or 46% of the load spectrum, whereas the 10 times POT extrapolated time history shows the same issue from a range of  $330 \mu\text{m}/\text{m}$  or 67% of the spectrum. As expected, the load spectra of the original sample and POT time domain extrapolation match below the threshold. The minute deviations below the threshold are from normalization, which results in a smoothing effect. The limiting RFM approach gives a smooth normalized spectrum up to load cycles with extreme ranges since the extrapolation is performed on the upcrossing spectrum, normalized to 1 km and smoothed using aKDE.

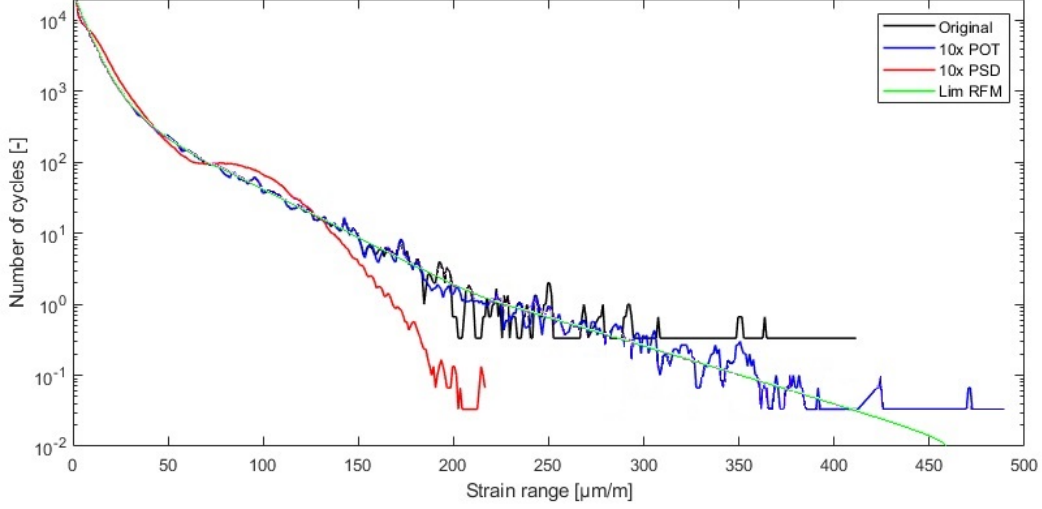


Figure 16: Normalized load spectrum for a 20% training sample, 10 times POT extrapolation, 10 times PSD extrapolation, and limiting RFM . All cycles are normalized to the number of cycles to occur in one signal length of the original sample. Zero values are not plotted for readability.

### 3.5.2 Fatigue Damage Error

The fatigue damage of the time domain methods are computed from the load spectra using equations 1, 2, and 3. The frequency-domain models calculate fatigue damage using the spectral moments calculated from the sample PSD and PSD-envelope using equations 28, 30, and the model specific equations, see section 2.2. Since the objective was to minimize the input data while still achieving satisfactory accuracy in the final fatigue damage calculations, the length of the input time history is varied to assess the robustness of the extrapolation method. The four samples  $T_1 - T_4$  represent 10%, 20%, 40%, and 100% of the training data, which for this specific military vehicle corresponds to  $\frac{1}{600}, \frac{1}{300}, \frac{1}{150}, \frac{1}{60}$  of the annually driven off-road km's. The first row with the mileage extrapolation is normalized to the damage from the longest time history, i.e.  $D_4$ . The error for each sample is based on the benchmark for each time history length, which is the fatigue damage of the mileage extrapolation (ME). All parameters are optimized separately for each time history as described in the previous sections. The error is determined as:

$$E_i = \frac{D_{ij} - D_{iME}}{D_{iME}} \times 100 \quad (43)$$

In expression 43 the index  $i$  represents the corresponding input time history varying from 1-4, and  $j$  indicates one of the eight methods used. The relative fatigue damage and errors from the eight fatigue damage models are given in table 7. The fatigue damage from the PSD-envelope is only reviewed in validation since the PSD-envelope does not vary and thus gives a fixed damage rate.

Method	$D_1$	$E_1$ [%]	$D_2$	$E_2$ [%]	$D_3$	$E_3$ [%]	$D_4$	$E_4$ [%]
ME	0.6807	n.a.	0.8722	n.a.	1.0308	n.a.	1	n.a.
POT	0.7598	11.63	0.9238	5.92	1.0988	6.60	1.0456	4.56
Lim RFM	0.8181	20.20	0.9269	6.28	1.1001	6.73	0.9947	-0.532
OC	0.8657	27.18	0.9989	14.53	1.2497	21.24	1.2060	20.60
SM	0.5911	-13.16	0.7221	-17.20	0.8814	-14.49	0.8401	-15.99
a75	0.7679	12.81	0.9212	5.62	1.1095	7.64	1.0618	6.18
TB3	0.7419	8.99	0.8769	0.54	1.0674	3.56	1.0173	1.73
DK	0.8045	18.19	0.9619	10.28	1.1337	9.99	1.1120	11.20
ZB	0.7662	12.56	0.9185	5.308	0.9371	-9.09	0.9226	-7.74

Table 7: Relative fatigue damage  $D_i$  and error  $E_i$  comparison between time-domain and frequency-domain fatigue damage models for four input signal lengths representing ; 1) 10% , 2) 20% , 3) 40%, and 4) 100% of the 90 km training dataset.

Fatigue damage in the time domain is underestimated up to 32% when only using 10% of the training dataset for ME (i.e. without applying load extrapolation) compared to the full training dataset. The lack of extreme loads in the tail data when using a 10-20% fraction of the training dataset is also clearly visible as discontinuities in the load spectra of the ME and POT method. Furthermore, the POT method applied on 10% of the training dataset compensates the fatigue damage underestimation from 32% to an error of 24%, whereas the limiting RFM reduces the error to 18 %. A clear and logical trend is visible; the error between POT or limiting RFM and the ME reduces when a larger fraction of the training dataset was used. In addition, at least 40% of the training dataset was required for a satisfactory accurate fatigue damage estimation of <5% for both time-domain fatigue damage models. With the full training dataset as input, the limiting RFM approach gives a 4.5% overestimation, whereas POT showed an underestimation of 0.5%.

Results of the six frequency domain fatigue damage models show that Dirlik’s method performs well for 10-20 % of the training dataset but overestimates fatigue damage >10% for larger fractions of the training data. TB3 is the most accurate method and is robust when at least 20% of the training dataset is used for input. The minimum error for TB3 was found to be 0.5%. On the other hand, OC and SM give inaccurate overestimates. OC overestimates fatigue damage by 14-27% depending on the fraction of the training dataset used. Whereas, the SM method underestimates fatigue damage by 13-17%.

### 3.6 Validation

Validation is performed by using the validation dataset containing the remaining 180 km of unique strain measurements of the same vehicle and operating conditions driven in 9.23 hr. The load spectra, PSDs, and fatigue damage errors are used to validate the results. The validation dataset gives a total fatigue damage  $D = 4.9 \times 10^{-4}$  [-] and from 4 the fatigue life  $T = 18692$  hr based on confidential material parameters of the front axle assembly where the measurements were performed.

#### 3.6.1 Load Spectra

More data from rare and extreme loads results in a more continuous tail of the load spectrum, as shown in section 3.5.1. For the 20% training sample the load spectrum only had sufficient load cycles up to 67% of the maximum strain range. Figure 17 shows a load spectra comparison including the validation dataset.

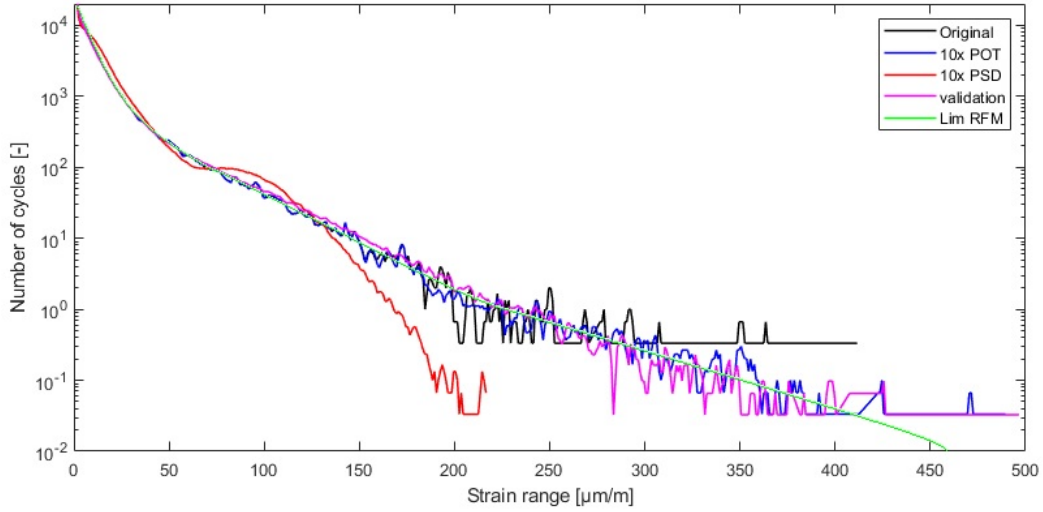


Figure 17: Normalized load spectrum of the 20% training sample, 10x POT extrapolation, 10x PSD extrapolation, limiting RFM and validation dataset. All cycles are normalized to the number of cycles to occur in one signal length of the original sample. Zero values are not plotted for readability.

Clearly, the 10 times POT extrapolation and the validation dataset show comparable load spectra. The validation load spectrum shows more cycles in the range of 180-250  $\mu m/m$ , yet fewer cycles between 280 and 360  $\mu m/m$ . A better graphical validation could be performed on a larger validation dataset with a continuous load spectrum above 380  $\mu m/m$ . In addition, after a 10 times POT extrapolation on the 40% and 100% training sample the extrapolated load spectrum contains more extreme load ranges than the validation dataset. As additional validation step, the limiting RFM is therefore compared to a factor 50 POT extrapolation, see appendix G for details. The high extrapolation factor provides a more smooth load spectrum to compare to the limiting RFM approach. The load spectrum of the limiting RFM approach is smooth for extreme ranges and fits the load spectrum of the validation data good up to 400  $\mu m/m$ . However, the estimation of the load spectrum tail from the extrapolated upcrossing spectrum shows an increasing uncertainty for smaller fractions of the training dataset. When calculating the fatigue damage from the load spectra, an underestimation or negative error to the validation dataset is expected for small training samples due to this effect.

### 3.6.2 PSD

The PSDs from the 20% sample of the training dataset, 10 times POT extrapolation, and the suggested military off-road envelope from section 3.4 are displayed with the validation PSD in figure 18. Since the PSD is the input for the frequency-domain fatigue damage models, the differences in fatigue damage estimations are caused from deviations between the PSD plots.

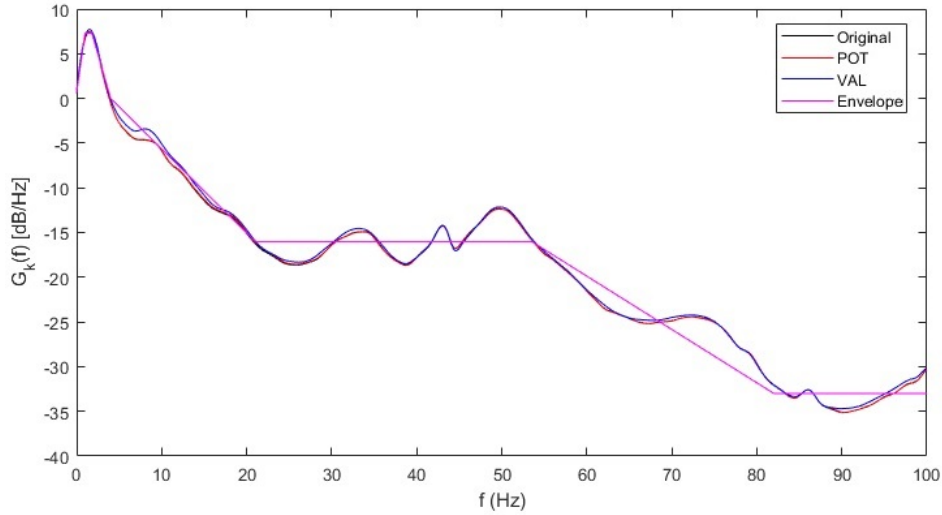


Figure 18: Single sided PSDs of the 20% training dataset sample, 10x POT extrapolated sample, off-road envelope and validation dataset.

The validation PSD shows a higher power around 10 Hz, 33 Hz, 70 Hz, and between 90-100 Hz. Earlier analysis proved that the damaging content is found below a frequency of 40 Hz. The deviations between the validation and other PSDs noticeable in figure 18 increase or decrease when using a smaller or larger sample from the training dataset, respectively. Furthermore, the PSD envelope follows the overall shape of the other PSD plots and contains the same energy in the frequency intervals 0-20 Hz, 20-50 Hz, and 50-100 Hz.

### 3.6.3 Fatigue Damage Error

With the load spectra and corresponding PSD as input for all fatigue damage models, the fatigue damage estimations are now compared to the validation data. The error from 43 is now calculated with the normalized validation fatigue damage as benchmark. Results are given in figure 19.

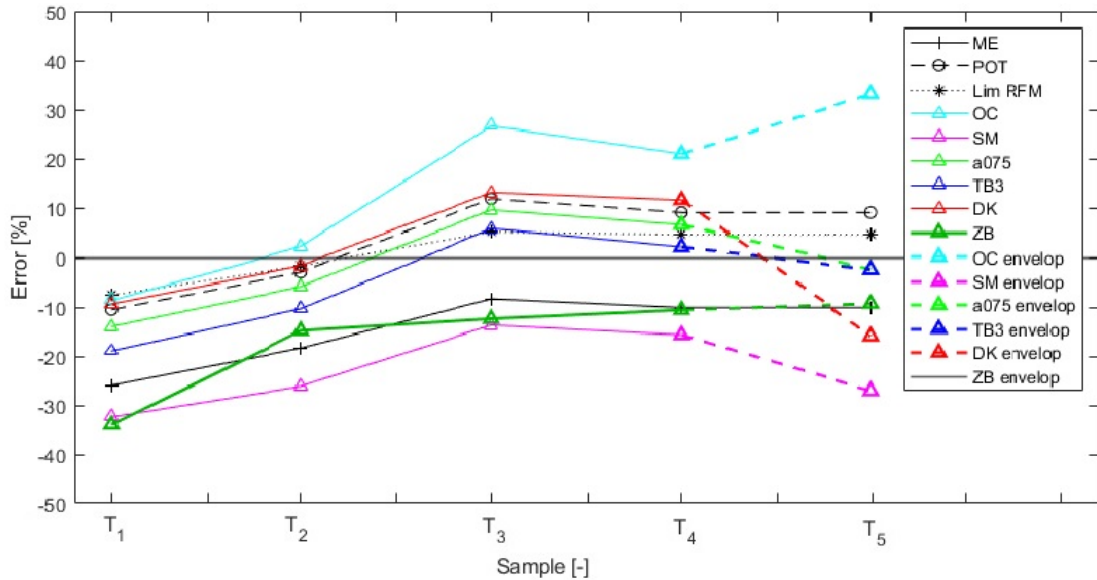


Figure 19: Error between fatigue damage estimation and the validation dataset on off-road strain measurements from a 4x4 military truck. Where  $T_1, T_2, T_3$ , and  $T_4$  contain 5%, 10%, 20%, and 50% of the data compared to validation, respectively.  $T_5$  corresponds to the suggested PSD-envelope.



### 3.7 Code availability

The case study was performed in MATLAB with data from the Dutch Army. From the main file dependencies to 14 other function files exist. Below the function files are listed and their function briefly explained. All 15 MATLAB m-files are uploaded to the [TU Delft Repository](#).

1. Msc\_main.m; main file to estimate life cycle fatigue damage from a time history.
2. Load\_data.m, preprocessing.m, and sniptool.m; Loads dataset, performs all preprocessing steps, and splits the dataset into training and validation subset.
3. Threshold\_selection.m; determines initial threshold for POT time history extrapolation.
4. EVT.m; determines final threshold, fits GPD to exceedances, and randomly resamples the exceedances.
5. limiting\_RFM.m, svvkernel.m; calculate upcrossing spectrum, extrapolate the upcrossing spectrum with a GPD fit to the tails, and estimate extreme RFM. Also applies aKDE estimation to the bulk of the RFM for smoothing.
6. PSD\_extrapolation.m, TimeseriesFromPSD.m; calculates PSD from the time sample, generates statistically equal time history of desired length.
7. RFMtoLoadSpectra.m; calculates RFM from time histories, applies Goodman correction, and calculates normalized load spectra.
8. CyclestoDamage.m; calculates fatigue damage from load spectra and Wohler curve.
9. Create\_PSD\_envelope.m; create off-road PSD envelope from training data.
10. PSDtoDamage.m; applies frequency-domain fatigue damage models to a given PSD.

## 4 Discussion

Goal of this thesis was to identify fatigue damage models which perform satisfactory (i.e.,  $<5\%$  error) for a minimized fraction of the training dataset. The sample of the training dataset was varied from 10% to 100% for eight fatigue damage models and the fatigue damage was calculated, after which the error to the full training dataset and validation dataset was determined to assess accuracy. In addition, for the time-domain models a load spectra comparison was executed. The results from section 3.5 and validation in section 3.6 mostly show expected trends and results in load spectra, PSDs, and fatigue damage error. For all fatigue damage models, the largest factor of influence on the final fatigue damage estimation is the presence of extreme load cycles in the data input. Ideally, the entire load spectrum is smooth after load extrapolation for the desired extrapolation factor. When only 10-20% of the training dataset is used, the load spectrum is discontinuous in the tail resulting in a large fatigue damage error. The 40%, and 100% training dataset samples result in a fatigue damage error below 5% (after compensation for the concentration of extreme loads in the 40% sample). Thus, the sample also contains sufficient extreme load cycles. The load spectrum of the 40% sample shows that 80% of the required load spectrum displays no large discontinuities. On the contrary to ME and POT methods, the limiting RFM approach always provides a smooth normalized RFM, which is easily extrapolated to the desired signal duration or distance. Yet, the accuracy of the limiting RFM fatigue damage estimation is within the 5% error tolerance above a 20% sample of the training dataset. For both time-domain load extrapolation methods the input is also determined by the threshold selection method and (non)parametric fit to the exceedances.

The ideal frequency domain fatigue damage estimation method is accurate independent of the PSD shape and material parameters. In this study, the scope is limited to military off-road vehicle loads, varying the fraction of input data and keeping the material parameters  $C$  and  $m$  constant. The influence of a different S-N slope exponent  $m$  and different  $S - N$  curve constant  $C$  on the fatigue damage estimation error is not investigated yet. For the spectral fatigue damage models, identical PSDs give identical fatigue damage rates. However, the PSD plots corresponding to the fractions of the training dataset shows lower energy in some regions compared to the validation PSD. Again, the negative error or fatigue damage underestimation increases for a smaller fraction of the training dataset used. Although validation is performed on a dataset only twice the size of the training dataset, results from all methods show that above a 40% fraction of the training dataset the validation error stabilizes, indicating the time history and PSD contain sufficient extreme loads for an accurate (i.e.  $<5\%$  error) fatigue damage prediction. Unexpectedly, the fatigue damage is overestimated for ME, POT, lim RFM,

OC,  $\alpha_{0.75}$ , TB3, and DK for the 40% fraction of the training dataset. Analysis of the training dataset show that a concentration of extreme loads was present in the shortened sample causing this effect. Accuracy of the frequency-domain methods also depends on whether the assumptions on which the method is developed are valid or not. For example, (semi)empirical approaches are often tuned for a certain range of material parameters and PSD shapes. Other approaches assume the loads to be random, stationary, and Gaussian. All six selected frequency-domain methods performed well on other typical wide-band automotive spectra in literature, yet OC and the SM method did not cope well with this specific off-road truck application compared to the other methods. TB3 and  $\alpha_{0.75}$  showed the lowest error in validation on >40% of the training dataset. Both methods are more recently revised (TB3 in 2006) or developed ( $\alpha_{0.75}$  in 2004) empirical methods fitted to a large variety of PSD samples. Finally, the validation error from the PSD envelope and PSD from the full training dataset show equivalent accuracy for TB3 and  $\alpha_{0.75}$ . Although, the PSD envelope underestimates damage whereas the training dataset overestimates the damage. Fatigue damage underestimation or a negative error is preferred in validation considering the training dataset contains less damaging load cycles than the validation dataset. This shows potential to use the envelope as input for dynamic modal analysis with these fatigue damage models.

## 5 Conclusions

The aim of this study was to compare accuracy of existing time-domain versus frequency-domain fatigue damage estimation models for military off-road vehicles whilst minimizing data acquisition time and costs. To do so, load extrapolation methods in the time-domain were optimized after which eight existing fatigue damage models were applied on a 10%, 20%, 40% and 100% fraction of a training dataset and an off-road PSD-envelope. The accuracy of the models is investigated by the error between the estimation and the normalized fatigue damage from the validation dataset. One time-domain and two frequency-domain models show an error <5% when >40% of the training dataset was used. None of the fatigue damage models performed satisfactory for all data fractions of the training set, i.e., <5% error in validation. Fatigue damage underestimation due to the lack of rare and extreme loads in the sample is reduced significantly when using >40% of the training dataset. Thus, a minimum dataset of 36 km or 13.3% of the total dataset was required in this case study for an accurate fatigue damage prediction. For at least 40% or 36 km of the training dataset, the limiting RFM is the most accurate and computationally efficient time-domain method. Furthermore, the limiting RFM approach provides a continuous load spectrum suitable for large extrapolation factors and is the most accurate method for >20% of the training dataset. The load spectrum from 40% of the training dataset was continuous up to 80% of the maximum value present in the measured time history and provided a validation error <5%. It is suggested to use this subjective graphic rule-of-thumb to assess if sufficient extreme loads are present in the measured signal to obtain a fatigue damage estimation error below 5%.

Regarding the frequency domain methods, TB3 is the most accurate method and is robust for >40% of the training dataset. The minimum error was found to be 2.1%, which is well below the 5% tolerance. The empirical  $\alpha_{0.75}$  method gives marginally poorer results in accuracy, as it systematically gives a higher fatigue damage prediction. The OC, SM, ZB, and DK methods are not recommended for military off-road application since the absolute errors in validation are in the order of 10-20%. Notably, ZB and DK approximate the load cycle amplitude pdf with a mixture model and both give poor prediction regardless of the training dataset fraction used. In addition, the validation error from the generic PSD-envelope is <5% for the best performing spectral methods, i.e. TB3 and  $\alpha_{0.75}$ . Therefore, the shape of the off-road envelope and approach to preserve the energy content within intervals is promising for further research. However, this envelope is specific to the 4x4 military truck and user profile from this case study.

### 5.1 Scientific and practical implications

Performance of a fatigue damage model is often determined by comparison to the ME benchmark in the time-domain, and the objective is to find a method which performs well for various PSD shapes or load spectra, material parameters and/or applications. For this thesis the case study was fixed to the specific application on military trucks used off-road. The performance of the models was assessed by investigating the effect of sample size on the error to the ME benchmark as time and costs due to data acquisition and validation are to be minimized. This study recommends the limiting RFM approach in the time-domain or TB3 and  $\alpha_{0.75}$  in the frequency-domain. These conclusions are in contrast to [19, 53], which found good results from the DK and ZB methods. However, [25, 27] showed that for higher values of  $m$  the error tends to increase up to 50% for DK. Furthermore, [25] made similar conclusions about the performance of the improved TB-method over 28 different fatigue loads including automotive spectra. Yet, found the ZB-method to be the most accurate for accelerated automotive loads which is not the case for off-road test profiles in this study. The results

from this thesis provide a solid base for application in life-cycle fatigue damage calculations within the Dutch Armed Forces. Data acquisition for the off-road section of the user profile is reduced to a minimum without compromising on accuracy of the fatigue damage prediction. As a result, validation of a military off-road prototype vehicle's durability is performed faster and the vehicle can be taken into service earlier. In addition, this thesis shows which estimation methods give the best results for the specific application to military off-road vehicles and quantifies the error to be made if incorrect assumptions are made about the damaging content within a measured sample.

## 5.2 Future work

In addition to this research, data acquisition time can be reduced further by complementing the extreme and rare events in the measured time history with measurements from an off-road test track where loads are induced at an accelerated rate correlated to the user profile. Essentially, the tail of the unique load spectrum is complemented with accelerated data which represent a larger distance of actual use. Also, the graphical methods used for initial threshold selection in the time-domain load extrapolation are subjective. The threshold selection is essential for the time-domain fatigue damage models and a widely discussed topic on it's own. For now, the MSE is minimized between the empirical and fitted PDF/CDF for possible thresholds around the graphically identified initial threshold. Further development of the automated threshold selection procedure is desirable. In addition, excluding the graphical methods for threshold selection and implementation of objective selection criteria is recommended, see e.g. [63] where a multi-criteria decision-making process is explained, which not only takes the error between empirical and fitted PDF/CDF into account, but also executes the  $\chi^2$ -test and proposes a method for objective selection of the lowest threshold that satisfies the conditions. Further research regarding the frequency-domain approaches is to be executed on the dependency on the material parameters  $C$  and  $m$  on the fatigue damage error since methods are often developed for a specific range. Other studies [26, 53, 64] show that generally the error increases for high values, i.e.  $7 < m < 12$ . Also, the relation between the loading capacity of the vehicle that is utilized and the effect on the load history is neglected in this study and still to be investigated. Finally, in order to implement the PSD-envelope on other user profiles further research is required to correlate the PSD shape of this case study to off-road surface conditions (sand, gravel, riverbeds, mud, snow, rocks, etc), vehicle parameters (axle load, wheel diameter, wheelbase, trackwidth, number of wheels, etc) and experimental conditions (speed, weather, driver style, etc). In addition, to perform dynamic modal analysis and estimate lifecycle fatigue damage from the PSD-envelope the frequency-response function  $H(\omega)$  of the vehicle used in this thesis and a different military off-road vehicle need to be determined. To conclude, it is recommended to apply the limiting RFM and/or TB3 method on lifecycle fatigue analysis of military off-road vehicles which requires data representing at least 13% of the desired lifespan for the prediction to be accurate within a 5% error tolerance.

# A Data Acquisition Datasheets

## A.1 Linear Strain Gauge

062AP



### General Purpose Strain Gages—Linear Pattern

GAGE PATTERN DATA					
<p>actual size</p>		<b>GAGE DESIGNATION</b> See Note 1, 3	<b>RESISTANCE (OHMS)</b> See Note 2	<b>OPTIONS AVAILABLE</b> See Note 3	
		EA-XX-062AP-120 ED-DY-062AP-350 EK-XX-062AP-350 <b>WA-XX-062AP-120</b> WK-XX-062AP-350 EP-XX-062AP-120 <b>SA-XX-062AP-120</b> <b>SK-XX-062AP-350</b> <b>SD-DY-062AP-350</b> WD-DY-062AP-350	120 ±0.15% 350 ±0.4% 350 ±0.15% 120 ±0.3% 350 ±0.3% 120 ±0.15% 120 ±0.3% 350 ±0.3% 350 ±0.8% 350 ±0.8%	W, E, L, LE, <b>P</b> E, L*, LE* W, <b>SE</b> W* <b>W*, SP35*</b>	
<b>DESCRIPTION</b> Widely used general-purpose gage. See also 062UW pattern. EK-Series gages are supplied with duplex copper pads (DP) when optional feature W or SE is not specified.					
<b>GAGE DIMENSIONS</b>		<b>Legend</b> ES = Each Section      CP = Complete Pattern S = Section (S1 = Section 1)      M = Matrix			
				inch	millimeter
<b>Gage Length</b>	<b>Overall Length</b>	<b>Grid Width</b>	<b>Overall Width</b>	<b>Matrix Length</b>	<b>Matrix Width</b>
0.062	0.114	0.062	0.062	0.26	0.16
1.57	2.90	1.57	1.57	6.6	4.1

GAGE SERIES DATA — See Gage Series datasheet for complete specifications			
Series	Description	Strain Range	Temperature Range
EA	Constantan foil in combination with a tough, flexible, polyimide backing.	±3%	-100° to +350°F (-75° to +175°C)
ED	Isoelastic foil in combination with tough, flexible polyimide film.	±2%	-320° to +400°F (-195° to +205°C)
EK	K-alloy foil in combination with a tough, flexible polyimide backing.	±1.5%	-320° to +350°F (-195° to +175°C)
WA	Fully encapsulated constantan gages with high-endurance leadwires.	±2%	-100° to +400°F (-75° to +205°C)
WK	Fully encapsulated K-alloy gages with high-endurance leadwires.	±1.5%	-452° to +550°F (-269° to +290°C)
EP	Annealed constantan foil with tough, high-elongation polyimide backing.	±10%	-100° to +400°F (-75° to +205°C)
SA	Fully encapsulated constantan gages with solder dots.	±2%	-100° to +400°F (-75° to +205°C)
SK	Fully encapsulated K-alloy gages with solder dots.	±1.5%	-452° to +450°F (-269° to +230°C)
SD	Equivalent to WD Series, but with solder dots instead of leadwires.	±1.5%	-320° to +400°F (-195° to +205°C)
WD	Fully encapsulated isoelastic gages with high-endurance leadwires.	±1.5%	-320° to +500°F (-195° to +260°C)

**Note 1:** Insert desired S-T-C number in spaces marked XX.

**Note 2:** Tolerance is increased when Option W, E, SE, LE, P, or SP35 is specified.

**Note 3:** Products with designations and options shown in **bold** are not RoHS compliant.

\*Options available but not normally recommended. See Optional Features data sheet for details.

## A.2 Bridge completion module

### MR-Series Bridge Completion Modules

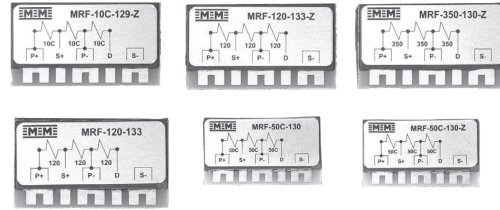


#### Information and Selection Chart

Strain gage instrumentation is readily available with built-in bridge completion resistors and “dummy” gages to accept quarter- and half-bridge strain gage input circuits. However, if the instrumentation at hand is not provided with these components, or if the measurement application does not permit their use, external bridge completion must be provided, and MR-Series Bridge Completion Modules can be an excellent choice in these applications.

MRF-Series Bridge Completion Modules employ Bulk Metal Foil Resistors. The resistors are specially processed to “match” the thermal expansion coefficient of the ceramic, resulting in a very low resistance temperature coefficient equivalent to  $\pm 0.15 \mu\epsilon/^\circ\text{F}$  ( $\pm 0.27 \mu\epsilon/^\circ\text{C}$ ) for the half-bridge circuits, and  $\pm 0.35 \mu\epsilon/^\circ\text{F}$  ( $\pm 0.63 \mu\epsilon/^\circ\text{C}$ ) for the dummy gages, over a temperature range from  $0^\circ$  to  $+200^\circ\text{F}$  ( $-18^\circ$  to  $+95^\circ\text{C}$ ). Maximum operating temperature range is  $-50^\circ$  to  $+250^\circ\text{F}$  ( $-45^\circ$  to  $+120^\circ\text{C}$ ).

Each module is covered with a special environmental protection system to ensure long-term stability. Each module is provided with foam tape for easy attachment to the test-part surface or at the instrumentation site, and gold plated copper terminals facilitate attachment of up to 22-gauge (0.64 mm dia.) leadwires.



Completing the bridge circuit at the strain gage site provides for a symmetrical, balanced leadwire system between the strain gage circuit and the instrumentation. This can reduce effects of noise pickup in the leadwire system in some environments. Where switch contacts, slip rings, or other mechanical connections are employed between the strain gages and measuring instrumentation, or when leadwires will be periodically disconnected from the measuring instrument, accuracy can be improved by completing the bridge at the measurement site. Bridge completion modules can be designed to meet special circuit requirements. Contact our Applications Engineering Department for a detailed discussion of your special needs.

CHARACTERISTICS		
MODULE TYPE AND FEATURES	BRIDGE EXCITATION (VOLTS)	
	RECOMMENDED	MAXIMUM
<b>MRF-350-127:</b> Provides a precision 350 $\Omega$ half bridge as well as 120 $\Omega$ and 350 $\Omega$ dummy gages. Recommended for use with half-bridge strain gage circuits of any resistance value, or with 120 $\Omega$ or 350 $\Omega$ three-wire quarter-bridge circuits. Size (including foam tape): 1.3 x 1.2 x 0.3 in (32.5 x 29.5 x 7.8 mm). Weight: 6g.	0.5–15 V 0.5–25 V	20 V (D120) 35 V (D350)
<b>MRF-350-127-Z:</b> RoHS compliant MRF-350-127	0.5–15 V 0.5–25 V	20 V (D120) 35 V (D350)
<b>MRF-10C-129:</b> Provides a precision 1000 $\Omega$ half bridge and a 1000 $\Omega$ dummy gage. Recommended for use with half-bridge strain gage circuits of any resistance value, or with 1000 $\Omega$ quarter-bridge circuits. High resistance extends battery life in battery-powered instrumentation, reduces strain gage self-heating, and permits higher bridge excitation voltage to improve signal-to-noise ratio. Size (including foam tape): 1.3 x 0.7 x 0.2 in (32 x 18.2 x 5.7 mm). Weight: 6g.	0.5–30 V	40 V
<b>MRF-10C-129-Z:</b> RoHS compliant MRF-350-127	0.5–30 V	40 V
<b>MRF-350-130:</b> Provides a precision 350 $\Omega$ half bridge and a 350 $\Omega$ dummy gage. Recommended for use with half-bridge strain gage circuits of any resistance value, or with 350 $\Omega$ three-wire quarter-bridge circuits. Size (including foam tape): 1.3 x 0.7 x 0.2 in (32 x 18 x 5.7 mm). Weight: 6g.	0.5–18 V	25 V
<b>MRF-350-130-Z:</b> RoHS compliant MRF-350-130	0.5–18 V	25 V
<b>MRF-350-128:</b> Provides a precision 350 $\Omega$ half bridge in a compact size for use with half-bridge strain gage circuits. Small size makes it ideal for attachment at the strain gage site on the test part in many applications. Size (including foam tape): 0.9 x 0.9 x 0.2 in (21.7 x 23.8 x 5.7 mm). Weight: 6g.	0.4–18 V	25 V

Half-bridge circuits in each module type are balanced to within  $\pm 0.005\%$ . Resistance tolerance on each dummy gage is  $\pm 0.02\%$ .

Information and Selection Chart

<b>CHARACTERISTICS</b>		
<b>MODULE TYPE AND FEATURES</b>	<b>BRIDGE EXCITATION (VOLTS)</b>	
	<b>RECOMMENDED</b>	<b>MAXIMUM</b>
<b>MRF-350-128-Z:</b> RoHS compliant MRF-350-128	0.4–18 V	25 V
<b>MRF-120-133:</b> Provides a precision 120 Ω half bridge and a 120 Ω dummy gage. Recommended for use with half-bridge strain gage circuits of any resistance value, or with 120 Ω three-wire quarter-bridge circuits. Size (including foam tape): 1.3 x 0.7 x 0.2 in (32 x 18.2 x 5.7 mm). Weight: 6g.	0.5–15 V	20 V
<b>MRF-120-133-Z:</b> RoHS compliant MRF-120-133:	0.5–15 V	20 V
<b>MRF-50C-130-Z:</b> Provides a precision 5000 Ω half bridge and a 5000 Ω dummy gage. Recommended for use with half-bridge strain gage circuits of any resistance value, or with 5000 Ω quarter-bridge circuits. High resistance extends battery life in battery-powered instrumentation, reduces strain gage self-heating, and permits higher bridge excitation voltage to improve signal-to-noise ratio. Size (including foam tape): 1.3 x 0.7 x 0.2 in (32 x 18 x 5.7 mm). Weight: 6g.	0.5–30 V	40 V
<b>MRF-50C-130-Z:</b> RoHS compliant MRF-50C-130:	0.5–30 V	40 V

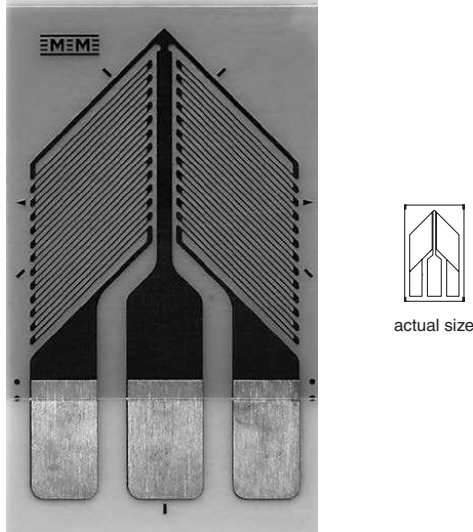

Half-bridge circuits in each module type are balanced to within  $\pm 0.005\%$ . Resistance tolerance on each dummy gage is  $\pm 0.02\%$ .

### A.3 Shear/Torque Rosette Strain Gauge



187UV / 187UVA

### General Purpose Strain Gages—Shear/ Torque Pattern

GAGE PATTERN DATA					
			<b>GAGE DESIGNATION</b> See Notes 1, 4	<b>RESISTANCE (OHMS)</b> See Note 2	<b>OPTIONS AVAILABLE</b> See Note 3
			CEA-XX-187UV-120 CEA-XX-187UVA-350	120 ±0.4% 350 ±0.2%	P2, SP35 P2, SP35
<b>DESCRIPTION</b> Two-element 90° rosette for torque and shear-strain measurement. Sections have a common electrical connection. Exposed solder tab area is 0.13 x 0.08 in [3.3 x 2.0 mm].					
<b>GAGE DIMENSIONS</b>		<b>Legend</b> ES = Each Section      CP = Complete Pattern S = Section (S1 = Section 1)      M = Matrix			inch millimeter
<b>Gage Length</b>	<b>Overall Length</b>	<b>Grid Width</b>	<b>Overall Width</b>	<b>Matrix Length</b>	<b>Matrix Width</b>
0.187 ES	0.560 CP	0.170 ES	0.320 CP	0.63	0.39
4.75 ES	14.22 CP	4.32 ES	8.13 CP	15.9	9.8

GAGE SERIES DATA — See Gage Series datasheet for complete specifications			
Series	Description	Strain Range	Temperature Range
CEA	Universal general-purpose strain gages.	±5%	-100° to +350°F (-75° to +175°C)

**Note 1:** Insert desired S-T-C number in spaces marked XX.

**Note 2:** Tolerance is increased when Option W, E, SE, LE, P, or SP35 is specified.

**Note 3:** Pattern names ending with "A" are built with Advanced Sensors Technology.



# A.4 Data Collection System

DEWE-5000





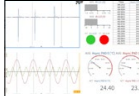
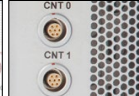


## DEWE-5000

- High-end benchtop all-in-one instrument
- 16 isolated DAQP analog inputs
- Flexible sidepanel for counters, sensor supply ...
- Up to 5 PCI slots for A/D and other cards (1394, ARINC, 1553...)



DEWE-5000 series	
Input specifications	DEWE-5000
Slots for DAQP/HSI/PAD modules	16
<b>Main system <sup>1)</sup></b>	
Total PCI slots	5 (4 full / 1 half length)
Hard disk	1000 GB
Data throughput	Typ. 70 MB/s <sup>2)</sup>
Power supply (max.)	90 to 264 V <sub>AC</sub>
Display	17.3" full-HD TFT (1920 x 1080)
Processor	Intel® Core™ i5
RAM	8 GB
Ethernet	2x 1 Gbit 2 LAN
USB interfaces	6
RS-232 interface	1
Operating system	64 bit Microsoft® WINDOWS® 7
Dimensions (W x D x H)	460 x 351 x 192 mm (18.1 x 13.8 x 7.7 in.)
Weight	Typ. 17 kg (37 lb.)
<b>Environmental specifications</b>	
Operating temperature	0 to +50 °C, down to -20 °C with prewarmed unit
Storage temperature	-20 to +70 °C
Humidity	10 to 80 % non cond., 5 to 95 % rel. humidity
Vibration <sup>3)</sup>	MIL-STD 810F 514.5, procedure I
Shock <sup>3)</sup>	MIL-STD 810F 516.5, procedure I

<sup>1)</sup> Please find current specifications in the latest price list  
<sup>2)</sup> Depends on the system configuration. Examples:  
 • DEWE-5000 with 4x DEWE-ORION-1624-200 and 1x DEWE-CAM01 = 72 MB/s  
 • DEWE-5000 with 2x DEWE-ORION-1624 + 4x DEWE-CAM01 = 60 MB/s  
<sup>3)</sup> Tested with Solid State Disk

<p><b>Needed to complete the system</b></p> <p>DEWE-ORION "A/D Boards" offer simultaneous sampled analog inputs, synchronous digital I/Os, high-performance counters and high-speed CAN interfaces. DAQP signal amplifiers and software are needed as well.</p>	<p><b>Options to expand the system</b></p> <p>Add further "Interface Cards" like ARINC-429, 1553, and analog output or special "Sensors" like synchronized video, industrial encoders (RIE-360) or GPS.</p>				
 <p>A/D card</p>	 <p>DAQP</p>	 <p>Software</p>	 <p>CNT2-LEMO</p>	 <p>VIDEO</p>	 <p>CAN</p>

DEWE-5000

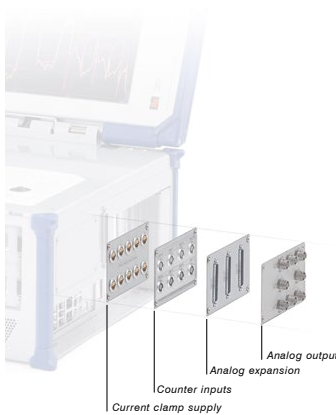


DEWE-5000

### DEWE-5000

Most flexible model, prepared for DAQP **isolated** analog input amplifier modules. DAQP conditioners offer highest bandwidth, great accuracy, different input ranges and integrated filters. Besides the single channel modularity – a module easily can be changed by the user at any time – the main advantage of these modules is the high galvanic isolation which ensures safe measurements, high quality results and make them almost indestructible. See chapter "Signal Conditioning" for details.

Max. channel count	ANALOG	16 DAQ modules
	DIGITAL	I/O card & counter & CAN



### Flexible side panel

The DEWE-5000 series instruments offer a flexible side panel prepared for adding additional connectors.

The most popular use of this panel is adding Lemo sockets for counter / encoder inputs. However, there are many different versions like multiple Binder 712 power supply connectors for current transducers, BNC sockets for analog outputs, multi-pin Sub-d sockets for additional analog inputs ...



DEWE-5000 side view

Due to the high number of available PCI slots the connection of additional interfaces like CAN bus, ARINC-429, Firewire-1394 etc. is done directly via the slot panel.

- Side panel with 10 connectors for powering current transducers
- 2 CAN interfaces on slot panel
- 2 FireWire interfaces on slot panel

## Example Configurations



**5000-PS-BAT**  
Optional battery power supply with UPS function

System options and upgrades for DEWE-5000 series	
Options	Description
BAT-89WH	Lithium-Ion battery, 14.4 V, 89Wh, max. 8A
BAT-CHARGER-1	Desktop battery charger for 1 battery, incl. external AC adaptor
BAT-CHARGER-4	Desktop battery charger for 4 batteries, incl. external AC adaptor
PS-BAT-REMOTE-ON	Special add-on for the battery power supply, one extra connection with a wake-up signal is required
DEWE-DCDC-24-300-ISO	External DC/DC converter with isolation, input: 11 to 32 VDC, output: 24 VDC, 300 W
5000-PS-BAT	Battery power supply with UPS function, 18 .. 24 V <sub>DC</sub> non-isolated input, incl. external AC adaptor, 3 slots for hot-swappable batteries, 3 batteries for appr. 2 hours operation included
Upgrades	Description
5000-CPU-UP-I7	Upgrade of PC for DEWE-5000 series to Intel® Core™ i7 processor
RAM-8GB-16GB	Upgrade from 8 GB to 16 GB RAM (total)
HDD-1T-SSD-256G	Upgrade to industrial grade 256 GB solid state disk (replaces 1 TB harddisk)
HDD-1T-SSD-1T	Upgrade to industrial grade 1 TB solid state disk (replaces 1 TB harddisk)

## Popular Accessories



Internal 256 GB Solid State Disk for maximum reliability



Accessory: 5000-CSMK1



Option 5000-DC-12V  
Internal 9 .. 18 V<sub>DC</sub> power supply including external AC adaptor.



Option BAT-CHARGER-1 and BAT-CHARGER-4



A carrying bag is available

## Channel Expansion

Signal conditioning for slow signals is added by connecting EPAD2 series modules to the systems EPAD interface.

For expanding the number of dynamic channels there are three choices:

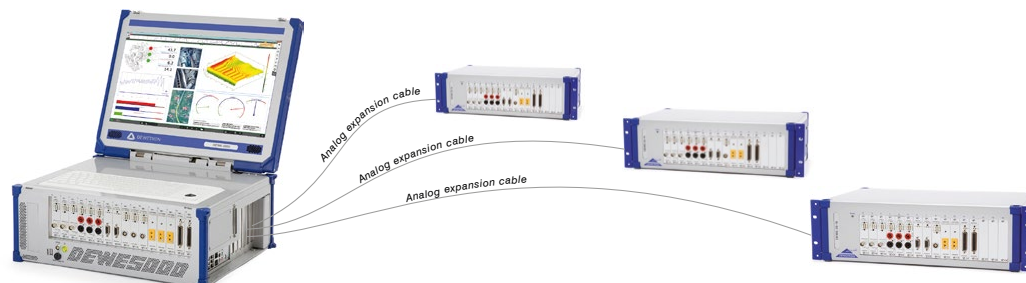
**Analog cable:** Additional A/D boards are installed into the basic instrument and external signal conditioning, e.g. DAQ modules in a DEWE-30 chassis, is connected by means of an analog signal cable.

**PCI expansion:** A PCI-HOST card is installed into the basic instrument and external signal conditioning, e.g. DAQ modules in a DEWE-50 chassis, is connected by means of a PCI cable.

**DEWE-NET:** Several instruments are connected via Ethernet. Each unit requires an ORION-SYNC option. For short distances a sync cable is used if the units are far from each other a sync interface like DEWE-CLOCK is used.

## Example

Analog expansion standard 2 m | optional up to 50 meter



DEWE-5000 with DEWE-30-16 signal conditioning chassis; DAQP modules for voltage, ICP®, bridge, strain ... measurement



## B Off-road terrain and test track examples

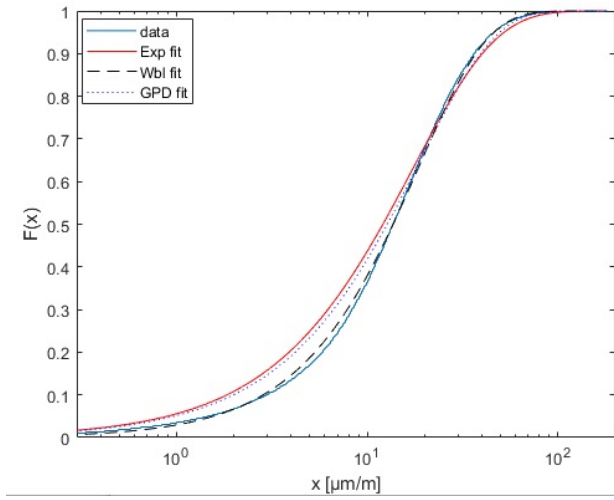


Figure 20: Selection of surfaces of the Millbrook proving ground[59]

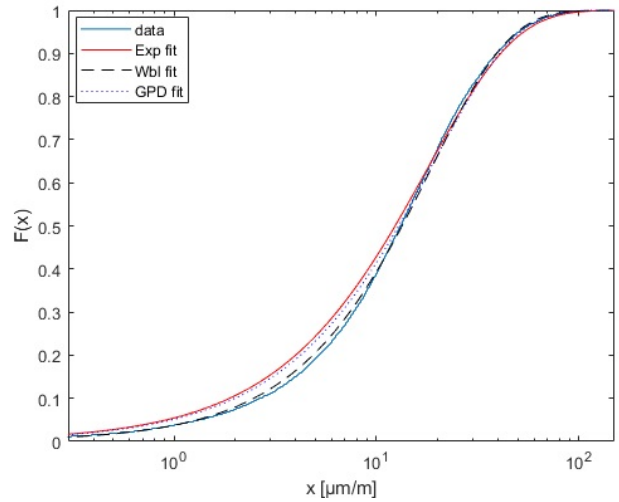


Figure 21: Selection of surfaces available on the Polygon Testing Grounds [60]

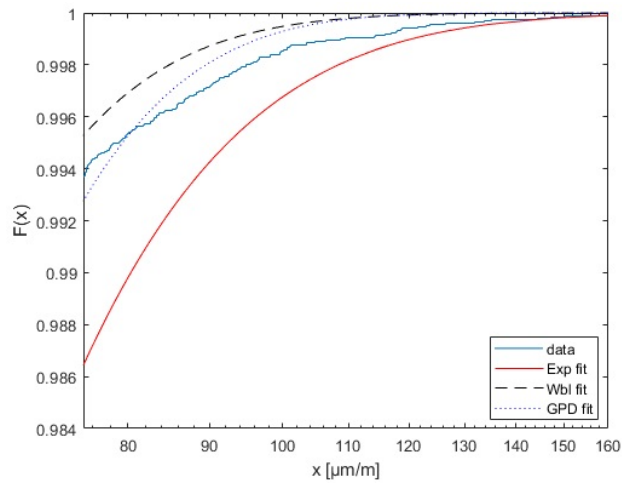
C Parametric fit on full 20% training sample, i.e.  $u = 0\mu m/m$



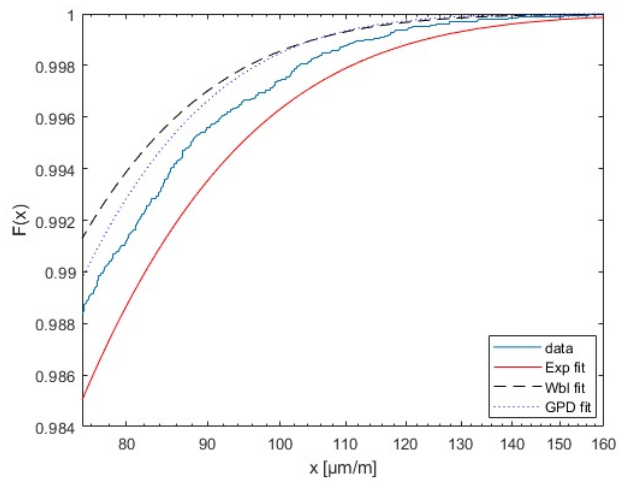
(a) CDF of positive exceedances for  $u = 0$



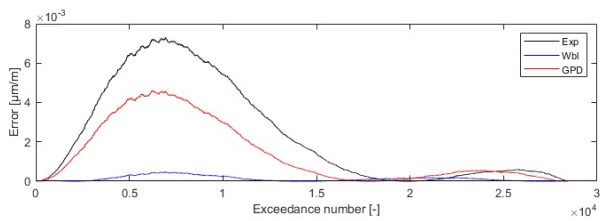
(b) CDF of negative exceedances for  $u = 0$



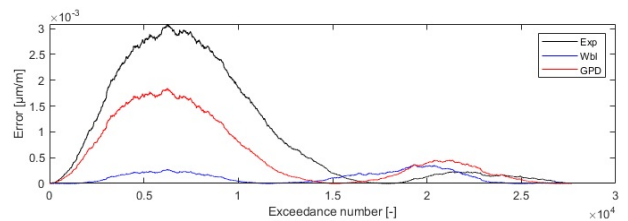
(c) Tail fraction of fig 22a



(d) Tail fraction of fig 22b



(e) Squared Error for positive exceedances with  $u = 0$



(f) Squared Error for negative exceedances with  $u = 0$

Figure 22: Parametric tail fit on CDF and squared error of both positive and negative exceedances with  $u = 0\mu m/m$  on the measured load history from an 4x4 military truck.

## D Parametric tail fit on 20% training sample with $u_{min} = -78\mu m/m$ , and $u_{max} = 95\mu m/m$

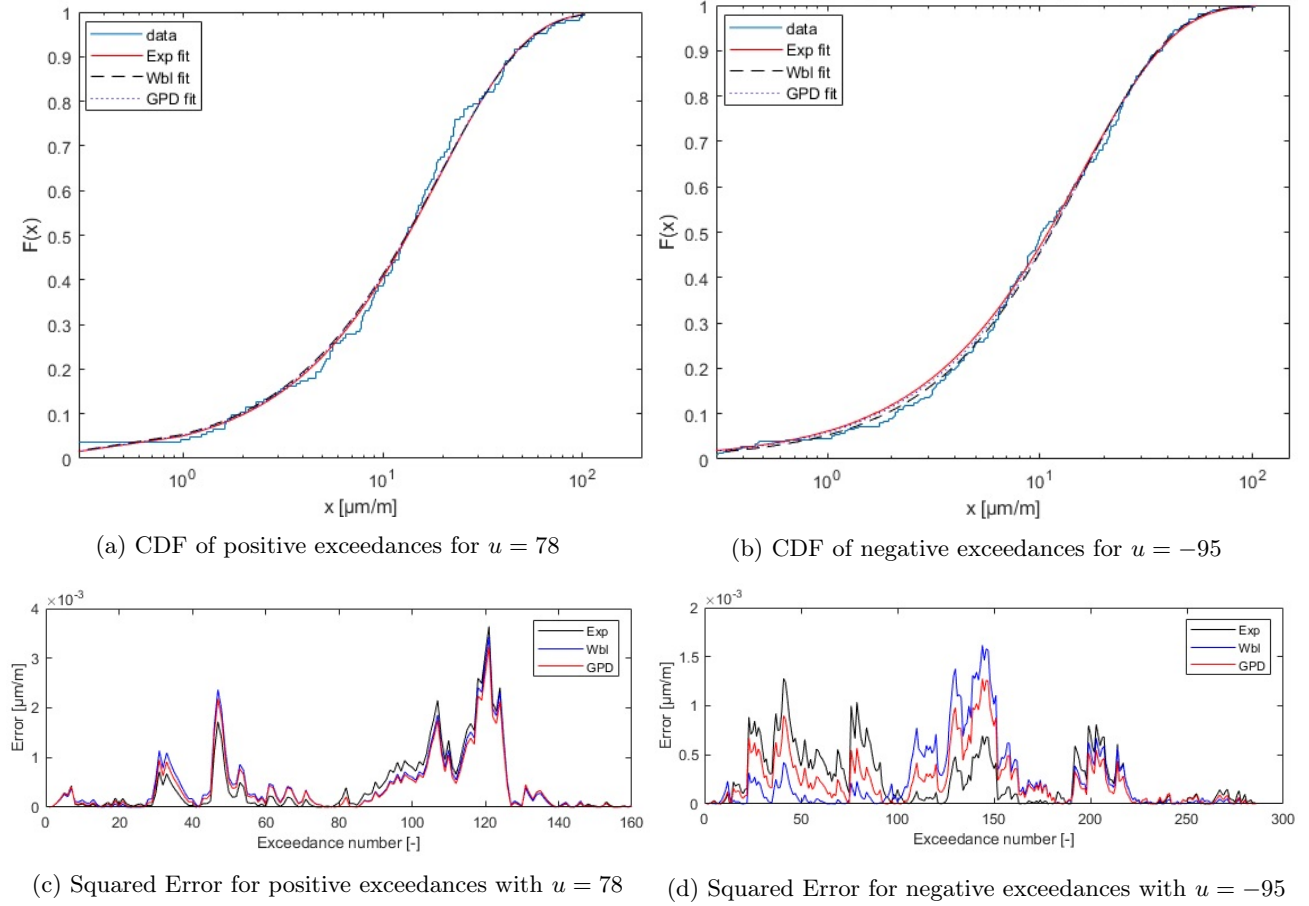
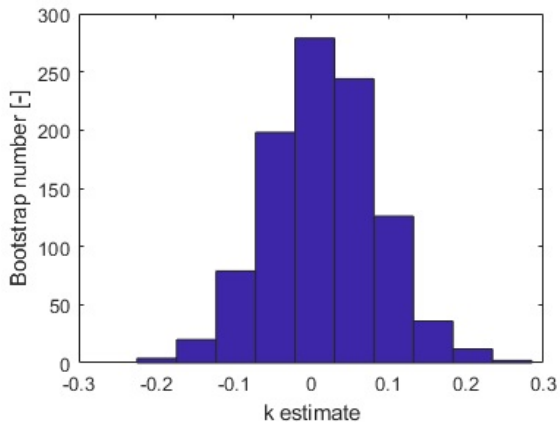


Figure 23: Parametric tail fit on CDF and squared error of both positive and negative exceedances with  $u_{min} = -95\mu m/m$  and  $u_{max} = 78\mu m/m$  on the measured load history from an 4x4 military truck.

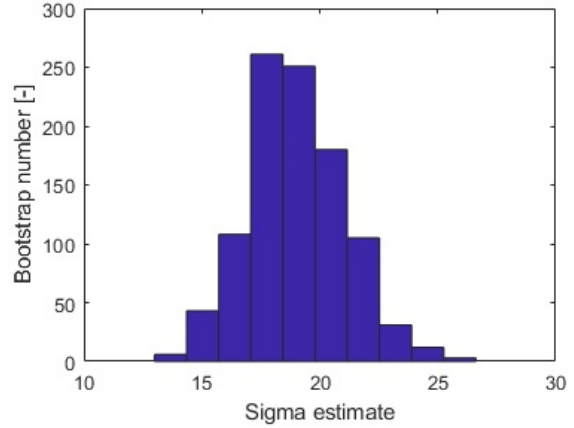
## E Diagnostic plots for parametric tail distribution

For EVT the goodness of fit on the GPD are graphically assessed using diagnostic plots. The MLE of the shape and scale parameters of the GPD should follow a normal distribution if the fit could be repeated with independent data. The asymptotic normality distribution is checked by plotting the 1000 fold bootstrap estimates of  $\kappa$  and  $\sigma$ . In addition, the quantile plots of the bootstrap estimates provide a more accurate way to detect deviations. For both the positive and negative GPD-fits the results are shown in figures 24, and 25.

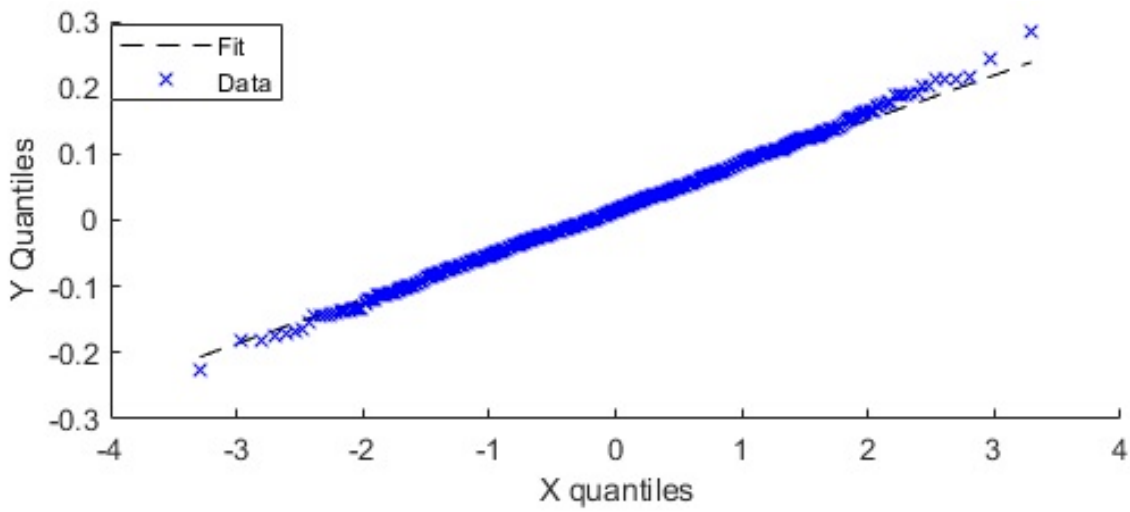




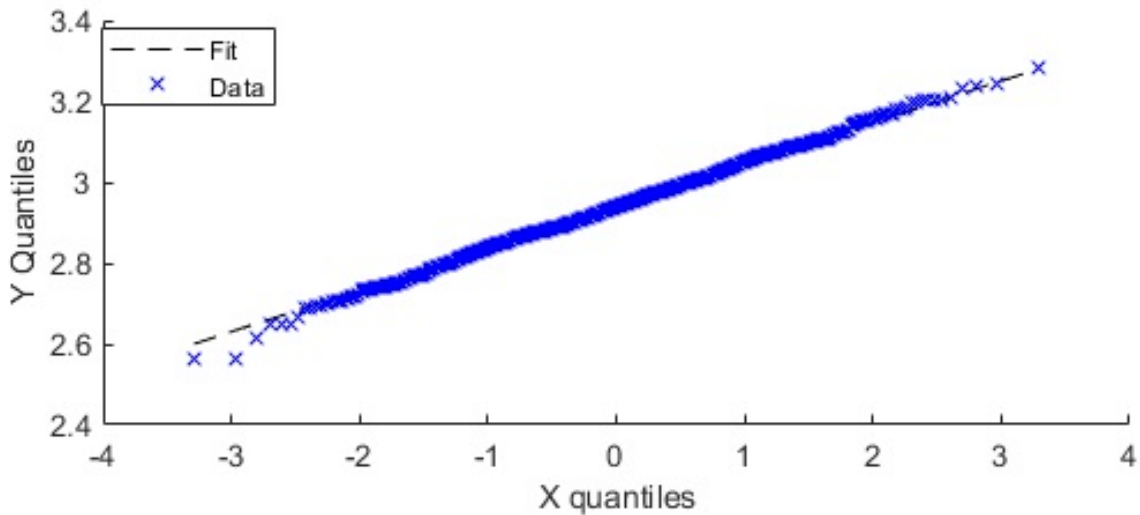
(a) Estimate of  $\kappa$  for 1000 fold bootstrapped data samples.



(b) Estimate of  $\sigma$  for 1000 fold bootstrapped data samples.



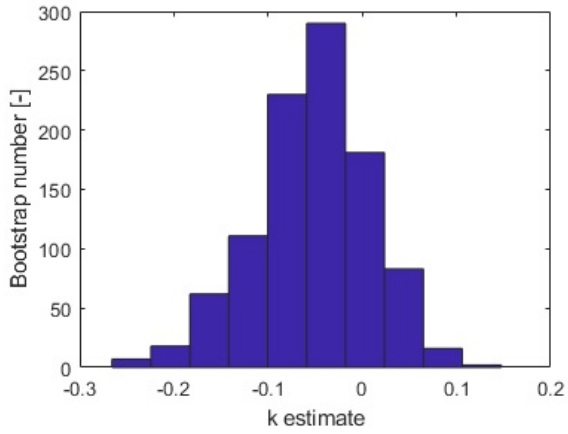
(c) Quantile plot for a 1000 fold bootstrap estimate of  $\kappa$ .



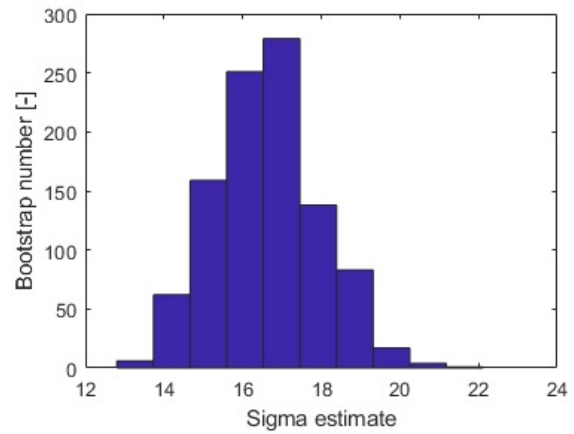
(d) Quantile plot for a 1000 fold bootstrap estimate of  $\log \sigma$ .

Figure 24: Diagnostic plots for the GPD fit on the positive exceedances of the 8x8 military truck off-road data.

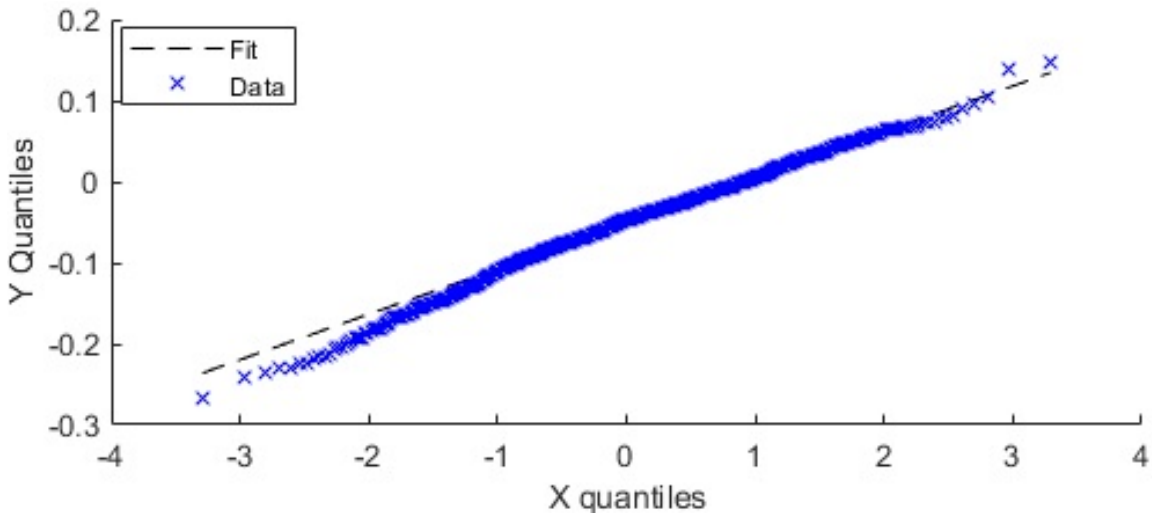




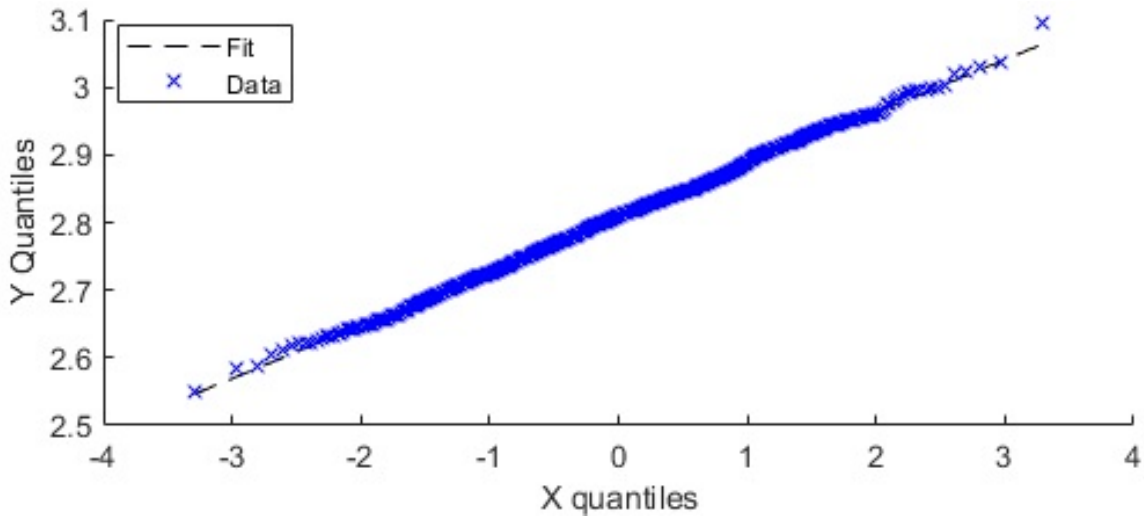
(a) Estimate of  $\kappa$  for 1000 fold bootstrapped data samples.



(b) Estimate of  $\sigma$  for 1000 fold bootstrapped data samples.



(c) Quantile plot for a 1000 fold bootstrap estimate of  $\kappa$ .



(d) Quantile plot for a 1000 fold bootstrap estimate of  $\log \sigma$ .

Figure 25: Diagnostic plots for the GPD fit on the negative exceedances of the 8x8 military truck off-road data.

## F PSD and generated time history

The PSD from the original time history, see figure 18, is used to generate a new time history of desired length, which gives an identical PSD in the frequency domain. The synthesized time history is compared to the original signal in figure 26. Clearly, the original time history has higher amplitudes, but overall contains the same frequency content. Furthermore, the load sequence of the original time history is not preserved in the synthesized time history, which can significantly affect fatigue damage [61, 65]. In the original time history an extreme load is followed with another slightly lower extreme value of opposite sign, which is logical as the vehicle suspension slowly dampens the disturbance. In the PSD generated time signal this causality is not taken into account.

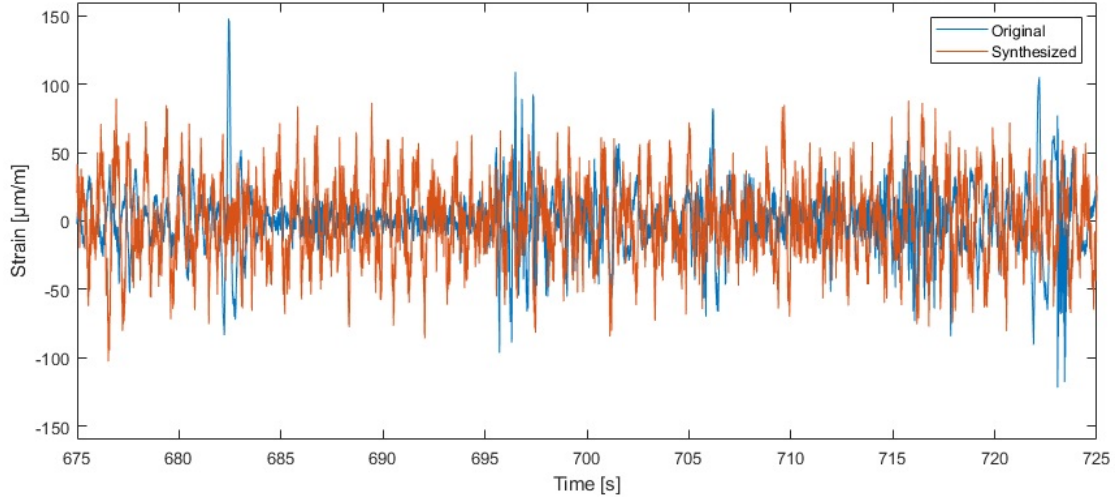


Figure 26: Section of the original measured time history and the time history generated from the PSD.

## G Limiting RFM validation

If sufficient data is available the load spectrum is smooth and suitable for large extrapolation factors using the mileage extrapolation method. However, for very limited input data the accuracy depends on the fitted distribution to obtain a smooth load distribution or RFM for extreme values. The time-history POT method was only used for an extrapolation factor of 10, leading to a load spectrum which was smooth up to  $250 \mu\text{m}/\text{m}$  or around 50% of the total spectrum. We strive to reach at least 80%, which is achieved with an extrapolation factor of 50 on the original time history thereby making it comparable with the validation data and limiting RFM approach. Results are shown in figure 27. Both the 50x POT and limiting RFM extrapolated load spectra show good agreement with the validation data. Considering the load spectrum of the validation data lacks data above  $425 \mu\text{m}/\text{m}$  we assume the corresponding fatigue damage for even the validation data is slightly underestimated. Thus both methods showing a higher fatigue damage estimation compared to the validation is expected since they complement the load spectrum, see also figure 19. Again, the limiting RFM approach is preferred as it shows good agreement with both the validation load spectrum and comparable POT time history approach. In addition, high extrapolation factors make the POT time history method computationally unattractive.

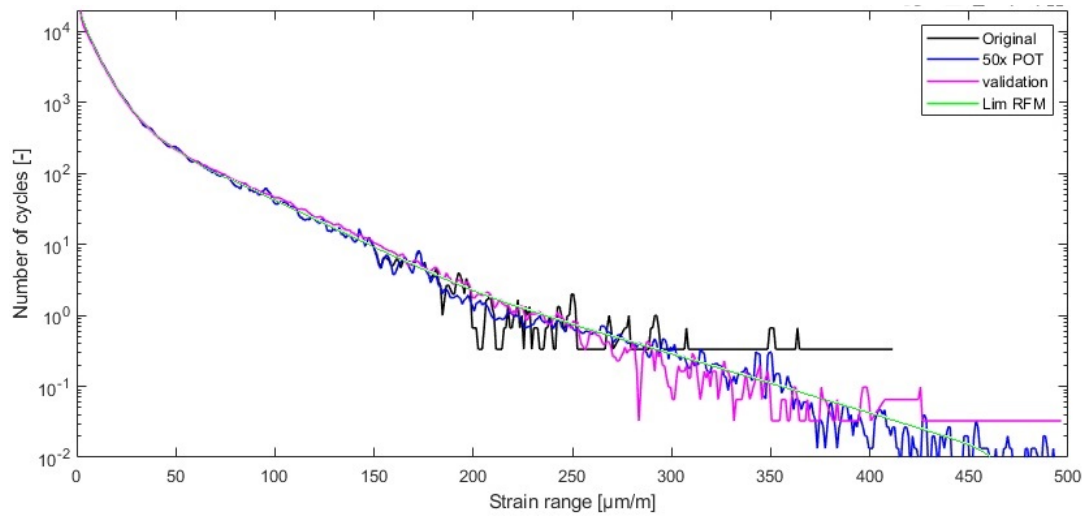


Figure 27: Normalized load spectra of the original sample, limiting RFM approach and 50x POT extrapolation.

## References

- [1] Heechang Shin, Robert Richardson, and Oredola Soluade. “An Analytic Framework for Assessing Automobile Sales Loss from Recalls: A Toyota Case Study”. In: *Lecture Notes in Business Information Processing* 115 (Jan. 2012), pp. 88–97.
- [2] MTS Systems Corporation. “Optimizing Durability Test Efficiency”. In: *Jaguar Land Rover*. 2014.
- [3] Georgia-Ann Klutke, Peter Kiessler, and M.A. Wortman. “A critical look at the bathtub curve”. In: *Reliability, IEEE Transactions on* 52 (Apr. 2003), pp. 125–129.
- [4] He J. et al. “Time domain load extrapolation method for CNC machine tools based on GRA-POT model”. In: *The International Journal of Advanced Manufacturing Technology* 103 (Aug. 2019).
- [5] Wu H. et al. “Application of kernel density estimation to extrapolating the fatigue loads on a high-speed train”. In: *International Journal of Vehicle Mechanics and Mobility* 58 (2020), pp. 1212–1225.
- [6] Jixin Wang, Yan Li, and Zhuji Jiang. “Non-parametric load extrapolation based on load extension for semi-axle of wheel loader”. In: *Advances in Mechanical Engineering* 9.3 (2017), p. 1687814017690073.
- [7] Thomas P. Johannesson J. “Extrapolation of Rainflow Matrices”. In: *Extremes* 4 (Sept. 2001), pp. 241–262.
- [8] Marko Nagode, Jernej Klemenc, and M. Fajdiga. “Parametric modelling and scatter prediction of rainflow matrices”. In: *International Journal of Fatigue* 23 (July 2001), pp. 525–532.
- [9] Ministry of Defense United Kingdom (MODUK). “Reliability and Maintainability (RM) Assurance Guide”. In: *DEF STAN 00-42*. 2016.
- [10] NATO International Staff. “Allied Environmental Conditions and Test Publication (AECTP)”. In: *AECTP-230, Edition 1*. 2009.
- [11] United States Department of Defense. “Environmental Engineering Considerations and Laboratory Tests”. In: *MIL-STD-810G Test Method Standard*. 2014.
- [12] United States Department of Defense. “Environmental Engineering Considerations and Laboratory Tests”. In: *MIL-STD-810H VIBRATION*. 2020.
- [13] Minor M.A. “Cumulative damage in fatigue”. In: *Journal of Applied Mechanics, ASME*, 12, A-159. 1945.
- [14] Wolfsteiner P. “Fatigue assessment of non-stationary random vibrations by using decomposition in Gaussian portions”. In: *International Journal of Mechanical Sciences* 127 (June 2016).
- [15] Halfpenny A. “A frequency domain approach for fatigue life estimation from Finite Element Analysis”. In: *International Conference on Damage Assessment of Structures*. 1999.
- [16] Light P.H. Wirsching M.C. “Fatigue under Wide Band Random Stresses”. In: *Journal of Structural Engineering, ASCE*, 106(7). 1980, pp. 1593–1607.
- [17] Chen K. Ortiz N.K. “Fatigue damage under Wide Band Random Stresses”. In: *presented at the 5th International Conference on the Applications of Statistics and Probability in Civil Engineering, Vancouver, Canada, 1987*. 1987.
- [18] Lutes C.E. Larsen L.D. “Predicting the Fatigue Life of Offshore Structures by the Single-Moment Spectral Method”. In: *Probabilistic Engineering Mechanics* 6 (June 1991), pp. 96–108.
- [19] Tovo D. Benasciutti R. “Spectral methods for lifetime prediction under wide-band stationary random processes”. In: *International Journal of Fatigue* 27 (Aug. 2005), pp. 867–877.
- [20] Dirlik T. “Application of computer in fatigue analysis”. In: (Jan. 1985).
- [21] Halfpenny A. “A frequency domain approach for fatigue life estimation from Finite Element Analysis”. In: *International Conference on Damage Assessment of Structures*. 1999.
- [22] Benasciutti T. Dirlik D. “Dirlik and Tovo-Benasciutti Spectral Methods in Vibration Fatigue: A Review with a Historical Perspective”. In: *Metals* 11 (Aug. 2021), p. 1333.
- [23] Wang J. et al. “A Review of the Extrapolation Method in Load Spectrum Compiling”. In: *Strojniški vestnik - Journal of Mechanical Engineering* 62 (Jan. 2016), pp. 60–75.
- [24] John Quigley, Yung-Li Lee, and Liang Wang. “Review and Assessment of Frequency-Based Fatigue Damage Models”. In: *SAE International Journal of Materials and Manufacturing* 9 (Apr. 2016).
- [25] Matjaž Mršnik, Janko Slavič, and Miha Boltežar. “Frequency-domain methods for a vibration-fatigue-life estimation – Application to real data”. In: *International Journal of Fatigue* 47 (2013), pp. 8–17. ISSN: 0142-1123.

- [26] Irvine C. Larsen T. “A Review of Spectral Methods for Variable Amplitude Fatigue Prediction and New Results”. In: *Procedia Engineering* 101 (Dec. 2015).
- [27] Han Q. et al. “A new frequency domain method for random fatigue life estimation in a wide-band stationary Gaussian random process”. In: *Fatigue Fracture of Engineering Materials Structures* 42 (July 2018).
- [28] Donaldson K.H. “Field Data Classification and Analysis Techniques”. In: *SAE Technical Paper*. Feb. 1982.
- [29] Endo M. Matsuichi T. “Fatigue of metals subjected to varying stress”. In: 1968.
- [30] Rychlik I. “A new definition of the rainflow cycle counting method”. In: *International Journal of Fatigue, Vol 9 issue 2* (Apr. 1987), pp. 119–121.
- [31] Kawakubo M. Kamaya M. “Mean stress effect on fatigue strength of stainless steel”. In: *International Journal of Fatigue* 74 (2015), pp. 20–29.
- [32] Marin J. “Interpretation of fatigue strengths for combined stresses”. In: *Proceedings of the International Conference on Fatigue of Metals* (Sept. 1956), pp. 184–195.
- [33] Zhu S.P. et al. “Mean stress effect correction in strain energy-based fatigue life prediction of metals”. In: *International Journal of Damage Mechanics* 26 (May 2016).
- [34] Pickands J. “Statistical Inference Using Extreme Order Statistics”. In: *Ann. Statist.* 3.1 (Jan. 1975), pp. 119–131.
- [35] de Haan A. Balkema L. “Residual Life Time at Great Age”. In: *The Annals of Probability* 2 (Oct. 1974).
- [36] MacDonald C. Scarrott A. “A review of extreme value threshold estimation and uncertainty quantification”. In: *Revstat Statistical Journal* 10 (Mar. 2012), pp. 33–60.
- [37] X et al Yang. “Threshold selection for extreme value estimation of vehicle load effect on bridges”. In: *International Journal of Distributed Sensor Networks* 14 (Feb. 2018).
- [38] Coles S. *An Introduction to Statistical Modeling of Extreme Values*. Springer, 2014. ISBN: 9781447136767.
- [39] Hill B. “A Simple General Approach to Inference About the Tail of a Distribution”. In: *The Annals of Statistics* 3 (Sept. 1975), pp. 1163–1174.
- [40] DuMouchel W. “Measuring Tail Thickness to Estimate the Stable Index Alpha: A Critique.” In: *The Annals of Statistics* 11 (Jan. 1983), pp. 1019–1031.
- [41] A. Ferreira, L. Haan, and L. Peng. “On optimising the estimation of high quantiles of a probability distribution”. In: *Statistics* 37 (Sept. 2003), pp. 401–434.
- [42] Johannesson P. “Extrapolation of load histories and spectra”. In: *Fatigue Fracture of Engineering Materials Structures* 29 (Mar. 2006), pp. 209–217.
- [43] Phillips M. Loretan P.C.B. “Testing the covariance stationarity of heavy-tailed time series: An overview of the theory with applications to several financial datasets”. In: *Journal of Empirical Finance* 1.2 (1994), pp. 211–248.
- [44] Rychlik I. “Rain-Flow-Cycle Distribution for Ergodic Load Processes”. In: *Siam Journal on Applied Mathematics - SIAMAM* 48 (June 1988).
- [45] Rychlik I. “Rainflow cycles in Gaussian Loads”. In: *Fatigue Fracture of Engineering Materials Structures* 15 (Apr. 2007), pp. 57–72.
- [46] Gramacki A. “Kernel Density Estimation”. In: Jan. 2018, pp. 25–62.
- [47] Shinomoto H. Shimazaki S. “Kernel bandwidth optimization in spike rate estimation”. In: *Journal of computational neuroscience* 29 (Sept. 2009), pp. 171–82.
- [48] Bishop N.W.M. “The use of frequency domain parameters to predict structural fatigue”. In: *PhD Thesis, University of Warwick* (1988).
- [49] Baker W. Zhao M.J. “On the probability density function of rainflow stress range for stationary Gaussian processes”. In: *International Journal of Fatigue* 14.2 (1992), pp. 121–135.
- [50] Cebon T.T. Fu D. “Predicting fatigue lives for bi-modal stress spectral densities”. In: *International Journal of Fatigue - INT J FATIGUE* 22 (Jan. 2000), pp. 11–21.
- [51] Tovo R. “Cycle distribution and fatigue damage under broad-band random loading”. In: *International Journal of Fatigue* 24 (Nov. 2002), pp. 1137–1147.
- [52] Tovo D. Benasciutti R. “Comparison of spectral methods for fatigue analysis of broad-band Gaussian random processes”. In: *Probabilistic Engineering Mechanics* 21.4 (2006), pp. 287–299.

- [53] Benasciutti D. “Fatigue analysis of random loadings”. In: *PhD thesis, University of Ferrara, Italy* (2004).
- [54] Moan Z. Gao T. “Frequency-domain fatigue analysis of wide-band stationary Gaussian processes using a trimodal spectral formulation”. In: *International Journal of Fatigue - INT J FATIGUE* 30 (Feb. 2008).
- [55] Lalanne C. *Fatigue Damage: Mechanical Vibration and Shock Analysis*. Jan. 2009.
- [56] Bendat J.S. “Probability functions for random responses”. In: *NASA report on contract NAS-5-4590*. 1964.
- [57] Micro-Measurements. *Stress Analysis Strain Gauges*. URL: <https://micro-measurements.com/stress-analysis-strain-gages>. (accessed: 06.01.2022).
- [58] LHM Instrumentation. *Dewetron DEWE-5000*. URL: <http://www.lhm-instrumentation.be/producten/dewetron-dewe-5000.html>. (accessed: 06.01.2022).
- [59] Millbrook. *Millbrook Proving Ground*. URL: <https://www.millbrook.co.uk>. (accessed: 09.06.2019).
- [60] TATRA Trucks. *TATRA Testing Grounds*. URL: <https://www.tatratrucks.com/your-tatra-partner/tatra-testing-grounds>. (accessed: 14.04.2019).
- [61] Pavlou D. “Loading Sequence Effects on Fatigue Damage Accumulation of Offshore Structures: A Deterministic Approach”. In: *36th International Conference on Ocean, Offshore and Arctic Engineering*. June 2017.
- [62] Patrick Moriarty, W. Holley, and S. Butterfield. “Extrapolation of Extreme and Fatigue Loads Using Probabilistic Methods”. In: (Jan. 2004).
- [63] Wang J. et al. “Determination of the Threshold for Extreme Load Extrapolation Based on Multi-Criteria Decision-Making Technology”. In: *Journal of Mechanical Engineering* 63.3 (2017), pp. 201–211.
- [64] V. Bouyssy, S.M. Naboishikov, and R. Rackwitz. “Comparison of analytical counting methods for Gaussian processes”. In: *Structural Safety* 12.1 (1993), pp. 35–57.
- [65] Pereira H. et al. “Analysis of Fatigue Damage under Block Loading in a Low Carbon Steel”. In: *Strain* 44 (Feb. 2008), pp. 429–439.